Absolute Deflection Measurements in a Micro- and Nano-Electromechanical Fabry-Perot Interferometry System

Roberto De Alba,[1, 2] Christopher B. Wallin,[1, 2] Glenn Holland,[1] Slava Krylov,[3] and B. Robert Ilic[1, a)]

[1)]*Physical Measurement Laboratory, National Institute of Standards and Technology, Gaithersburg, MD 20899, USA*

[2)]*Institute for Research in Electronics and Applied Physics, University of Maryland, College Park, MD 20742, USA*

[3)]*School of Mechanical Engineering, Faculty of Engineering, Tel Aviv University, Ramat Aviv 69978, Tel Aviv, Israel*

Fabry-Perot laser interferometry is a common laboratory technique used to interrogate resonant micro- and nano-electromechanical systems (MEMS/NEMS). This method uses the substrate beneath a vibrating MEMS/NEMS device as a static reference mirror, encoding relative device motion in the reflected laser power. In this work, we present a general approach for calibrating these optical systems based on measurements of large-amplitude motion that exceeds one half of the laser wavelength. Utilizing the intrinsic nonlinearity of the optical transduction, our method enables the direct measurement of the system's transfer function (motion-to-detected-voltage). We experimentally demonstrate the use of this technique to measure vibration amplitudes and changes in the equilibrium position of a MEMS/NEMS device using monolithic silicon nitride and silicon cantilevers as sample systems. By scanning the laser along a cantilever surface, we spatially map static and dynamic deflection profiles simultaneously, and then compare the static profile against results from a commercial optical profilometer. We further demonstrate extension of our calibration technique to measurements taken at small amplitudes, where the optical transduction is linear, and to those taken in the frequency domain by a lock-in amplifier. Our aim is to present a robust calibration scheme that is independent of MEMS/NEMS materials and geometry, to completely negate the effects of nonlinear optical transduction, and to enable the assessment of excitation forces and MEMS/NEMS material properties through the accurate measurement of the MEMS/NEMS vibrational response.

[a)]Electronic mail: robert.ilic@nist.gov

I. INTRODUCTION

Modern MEMS/NEMS experiments utilize mechanical resonators to push the limits of force and mass sensing[1–6], demonstrate novel electromechanical circuit applications[7–11], measure the structural properties of materials[12–14], and study quantum physics[15,16]. These devices have varied geometries including cantilevers, doubly-clamped bridges, microdisks, and membranes, and are made from materials ranging from standard semiconductors and dielectrics (e.g. Si, GaAs, SiN)[17–19] to carbon nanotubes[4,20], graphene[14,21,22], and other atomically-thin films[23–26].

Fabry-Perot laser interferometry is a popular and robust technique for probing MEMS/NEMS devices[1,9,13,14,21,23–36] because it is non-invasive – requiring no electrical contact to the test sample – and provides exceptional motion sensitivity (roughly $10\,\mathrm{fm}\cdot\mathrm{Hz}^{-1/2}$ in Ref. 30). Furthermore, a typical laboratory setup can function over a wide frequency range, from a few Hz to hundreds of MHz, and is compatible with any MEMS/NEMS material that is partially optically transparent. This requirement is easily satisfied with typical device thicknesses on the order of 100 nm or less. Additionally, the interferometry technique utilizes a partially reflective substrate as a static reference mirror beneath the MEMS/NEMS resonator. Doing so provides common-mode noise rejection when compared to interferometers that use an external reference mirror.

An important feature of the Fabry-Perot interferometry setup is the tight focus of the laser used to detect MEMS/NEMS motion. This focus is typically achieved using a microscope objective, and results in a spot diameter of $w \approx 1\,\mu$m to $5\,\mu$m over which the device motion is effectively averaged. For devices with lateral dimensions much larger than the focused laser spot, scanning the spot location provides a means to image the vibrational modes of the device. A noteworthy example of this technique appears in Ref. 30, in which multiple modes of a $20\,\mu$m-wide SiC microdisk were imaged using only its thermal Brownian motion for excitation. This result, as with most reported measurements, is made possible by the linearity of the optical transduction when vibration amplitudes are much smaller than the laser wavelength, λ.

Despite the simplicity and sensitivity of this optical technique, it suffers from two main shortcomings: Firstly, motion transduction is highly nonlinear when MEMS/NEMS motion exceeds $\lambda/4$. This artificially constrains MEMS/NEMS experiments to small vibration amplitudes, limiting the signal-to-noise ratio and therefore sensitivity of some mass sensing devices. Secondly, because the reference mirror cannot be moved independently, there is no simple or established technique for calibrating device motion. For this reason, vibration amplitudes are typically re-

ported in arbitrary units, and only the resonant frequency is known with certainty. This single datum can be used to estimate one mechanical parameter of the system (e.g. total mass, internal stress, elastic modulus, or applied force), assuming all other relevant parameters are known. A calibrated optical system would enable measurement of resonator's vibration amplitude and static deflection, providing additional data for the assessment of material properties and loading conditions.

Existing methods for calibrating deflections in MEMS/NEMS measurements involve either measuring Brownian motion[29,36–38] or measuring nonlinear behavior[9,36], such as the critical vibration amplitude at which a Duffing response becomes multistable. Both require extensive theoretical modeling, introducing sources of error, and both are highly dependent on device materials and geometry. Furthermore, neither of these calibration methods provides information about the static deflection of the MEMS/NEMS device. Nor do they address the issue of nonlinear optical transduction. Utilizing the nonlinearity of an optical system's transfer function, henceforth referred to as its interference pattern, to calibrate motion has been attempted, but typically under the assumption that the interference pattern is sinusoidal[32,36,39].

The calibration scheme we present here is independent of both MEMS/NEMS materials and geometry and makes no assumptions regarding the system's interference pattern. Our method allows for a direct measurement of the interference pattern of an arbitrary MEMS/NEMS system by simply measuring reflected laser power in the time domain and applying a mathematical transformation. If the device motion spans a full interference fringe, a calibration can then be obtained by using the peak-to-peak width of this fringe as a reference for $\lambda/2$. Furthermore, our approach fully compensates for nonlinear optical transduction, and allows for the direct comparison of large- and small-amplitude data to discern changes in both vibration amplitude and static deflection.

II. EXPERIMENTAL SETUP

A diagram of our experimental setup is shown in Fig. 1(a). The essential components are the laser source with a wavelength $\lambda \approx 640\,\text{nm}$, a long-working-distance objective (LWDO), a beam splitter (BS), a polarizing beam splitter (PBS), and a high-speed photodetector (PD). All of the remaining optics serve to either improve the signal-to-noise ratio of the system or enable live imaging of the MEMS/NEMS sample with a digital camera. A variable beam expander (VBE) adjusts the beam diameter to match the objective aperture, minimizing the focused spot size. A

$\lambda/2$ waveplate (WP) in the beam path ensures that the PBS transmits $\approx 100\%$ of light from the laser source. Upon exiting the PBS, this light encounters a $\lambda/4$ WP that circularly polarizes it before entering the LWDO. After reflection from the MEMS/NEMS sample, a second pass through the $\lambda/4$ WP reverts the light to a linear polarization, rotated 90° relative to the original polarization, for $\approx 100\%$ reflection by the PBS into the PD. Compared to a $50/50$ BS, the PBS therefore roughly doubles the measured signal strength for a fixed laser power incident on the sample. The image relayed to the digital camera is magnified by a zoom lens (ZL), and the MEMS/NEMS sample is on a motorized translation stage (MTS), enabling computer control of the sample position. The sample is situated inside a high-vacuum chamber (HVC) with optical access and mounted on a piezoelectric disk to inertially drive the MEMS/NEMS motion. The piezoelectric drive signal is provided by a lock-in amplifier (LIA), and the photodetector voltage is measured by the same LIA or by an oscilloscope (OS). All experiments were performed at a pressure below 10^{-4} Pa to minimize viscous drag.

Figure 1(b) demonstrates a typical interferometry measurement of a MEMS/NEMS resonator in the large-amplitude regime, where peak-to-peak motion exceeds $\lambda/4$. In this case, the resonator is a silicon nitride cantilever (Fig. 1(a) inset) being driven inertially. The laser was focused near the cantilever free end, and the data was recorded using the LIA. The upper (lower) panel shows the response of the cantilever to an upward (downward) sweep of the drive frequency, f. The cantilever response is plotted as V_1, the voltage amplitude detected by the LIA at the drive frequency. Both panels demonstrate several localized peaks of varying width and depth that originate from the nonlinear optical transduction. The peak width, particularly in LIA measurements, has a non-trivial relation to the MEMS/NEMS vibration amplitude, R, which will be discussed in Sec. V C. These optical transduction effects obfuscate the MEMS/NEMS motion, and to an unsuspecting experimenter could lead to a false notion of exotic device behavior. Figure 1(c) presents the same data after processing via the calibration scheme described in Sec. V C, clearly showing that the cantilever exhibits a standard Duffing-type mechanical response. Once the optical effects have been accounted for, the data's remaining asymmetry and hysteresis are consistent with a nonlinear mechanical spring force.

Throughout this work we utilize cantilevers that are $\approx 50\,\mu$m in length to study peak-to-peak motion that far surpasses λ. For all the results presented in the main text, the device is a monolithic cantilever composed of low-pressure chemical vapor deposited (LPCVD) silicon nitride. The width and thickness of this cantilever are approximately $10\,\mu$m and 200 nm, respectively. This

cantilever is separated from its underlying silicon substrate by a distance $h \approx 2\,\mu$m, as determined by the thickness of a layer of sacrificial silicon dioxide. In the Supplemental Sec. S1, we present results for a monolithic silicon cantilever of similar dimensions, and for a second silicon cantilever that is $\approx 2.5\,\mu$m in width. These cantilevers are intended to typify a generic MEMS/NEMS device, as optical interactions will be broadly similar for devices of different geometries.

III. CALIBRATION METHODS

The transduction in a MEMS/NEMS interferometry system can be described by $V_{\mathrm{PD}}(z) = GP_{\mathrm{in}}(z)$, where $V_{\mathrm{PD}}(z)$ is the voltage generated by the photodetector, G is the optical-power-to-voltage gain of the detector, and $P_{\mathrm{in}}(z)$ is the total power incident on the photodetector surface. Because this power is composed of reflections from each optical interface in the MEMS/NEMS system, it is a function of the resonator's out-of-plane displacement, z. Furthermore, because G is a fixed scalar dependent only on the efficiency of the detector at the given wavelength and on the amplifier circuitry, we interchangeably refer to $P_{\mathrm{in}}(z)$ and $V_{\mathrm{PD}}(z)$ as the 'interference pattern' of the MEMS/NEMS system.

In an ideal Fabry-Perot interferometer with parallel interfaces and optical plane waves, the interference pattern can be calculated straightforwardly and is perfectly periodic with respect to interface distance, with a period of $\lambda/2$. Under typical laboratory conditions, however, several complicating factors arise as shown in Figs. 2(a)–2(d). These include: 1) divergence of the laser beam on length scales comparable to the resonator-substrate gap, 2) the changing inclination angle of the MEMS/NEMS resonator during its motion, 3) reflected light outside the acceptance cone of the microscope objective, 4) optical diffraction around the lateral edges of the resonator, and 5) the laser beam's Gouy phase shift, which alters the apparent wavelength near the laser focus. Furthermore, $V_{\mathrm{PD}}(z)$ depends on the distance between the substrate and the laser's focal plane and on the photodetector alignment. The resulting interference pattern is only quasiperiodic, as demonstrated by the example in Fig. 2(e). Thus, there are many degrees of freedom in the optical system – many of which are difficult to measure or reproduce accurately. For this reason, although several previous studies have attempted to model the optical transduction of MEMS/NEMS systems using numerical simulations[35,40] or by assuming a perfectly sinusoidal interference pattern[32,36,39], we take the alternative approach of measuring $V_{\mathrm{PD}}(z)$ directly.

To extract $V_{\mathrm{PD}}(z)$, we measure the photodetector voltage as a function of time, t, and then map

t to z. This process assumes the following relation between variables:

$$z(t) = z_0 + R\cos(2\pi f(t - t_0)). \tag{1}$$

Here z_0 is resonator's static deflection, R is its vibration amplitude, and f is the drive frequency. Maximum deflection occurs at time $t = t_0$. Because the focused laser has a finite spot size $w \approx 5\,\mu$m on the MEMS/NEMS resonator, z should be thought of as the average deflection of the illuminated area, rather than the deflection directly at the laser center. Additionally, as we will discuss below, our technique can discern changes in z_0 between measurements (e.g. due to a change in loading conditions), but it cannot measure the total distance from the substrate. Therefore, while relative shifts in z can be measured, the choice of origin $z = 0$ in our interference patterns is arbitrary. Figure 2(e) demonstrates the relation between an interference pattern $V_{\mathrm{PD}}(z)$ and a simulated time-domain measurement $V_{\mathrm{PD}}(t)$.

Figures 3(a)–3(d) demonstrate our method of extracting $V_{\mathrm{PD}}(z)$ from a measured oscilloscope trace $V_{\mathrm{PD}}(t)$. This begins by mapping the time dimension onto a new dimensionless variable, u, defined by:

$$u = \cos\left(2\pi f(t - t_{\mathrm{TP}})\right). \tag{2}$$

Here, the time t_{TP} coincides with any turning point in the resonator's oscillation cycle and is determined by locating even symmetry points along the time axis (Fig. 3(a), arrows). Relative to t_0 in Eq. (1), these turning points all satisfy $t_{\mathrm{TP}} = t_0 + \frac{1}{2}NT$, where N is an integer and $T = f^{-1}$ is the period of oscillation. If N is even, u is related to z by $u = (z - z_0)/R$. If N is odd, this relation changes sign: $u = -(z - z_0)/R$. In either case, $u = 0$ always signifies the resonator's equilibrium position $z = z_0$, and $u = \pm 1$ correspond to the extremes $z = z_0 \pm R$.

Data after mapping t to u is shown in Fig. 3(b). Because of the linear relation between u and z, this mapped data $V_{\mathrm{PD}}(u)$ is visually identical to the desired interference pattern $V_{\mathrm{PD}}(z)$, as shown in Fig. 3(c). Depending on the choice of turning point t_{TP} in Eq. (2), the uncalibrated interference pattern $V_{\mathrm{PD}}(u)$ can be plotted as shown or mirrored along the $u = 0$ axis. By convention, throughout this work we plot interference patterns $V_{\mathrm{PD}}(u)$ and $V_{\mathrm{PD}}(z)$ so that the fringe contrast – i.e. voltage difference between neighboring peaks and valleys – decreases as u and z increase. This is because we have chosen positive z to correspond to motion away from the silicon substrate, and we assume that positive motion leads to a lower fringe contrast due to the beam divergence that occurs between the optical interfaces. We calibrate interference patterns $V_{\mathrm{PD}}(u)$ by one of two methods:

1. **'Peak-to-Peak' Method:** If the uncalibrated data $V_{\mathrm{PD}}(u)$ displays at least two peaks or two valleys, it is said to be in the large-amplitude regime ($R > \lambda/4$). Because of the quasiperiodic nature of the interference pattern, pairs of neighboring peaks (and pairs of valleys) are separated by a distance $\approx \lambda/2$, where each $\lambda/2$ span is referred to as an interference fringe. The dimensionless peak-to-peak distance Δu is measured, and the vibration amplitude can be determined from $R \approx \lambda/(2\Delta u)$. In an example such as Fig. 3(b), where many peaks and valleys are visible, the mean peak-peak and valley-valley distance is taken as Δu. To monitor changes in the static deflection z_0 between measurements, a single peak (or valley) can be chosen as reference, and its movement relative to the origin ($u = 0$) is monitored.

2. **'Stretch' Method:** For small-amplitude data ($R < \lambda/4$), a full interference fringe is not observed and $\lambda/2$ cannot be measured directly. In such a case, the uncalibrated data $V_{\mathrm{PD}}(u)$ is compared to a reference interference pattern $V_{\mathrm{ref}}(z)$. This is shown in Fig. 3(c). The uncalibrated data is shifted and scaled along the horizontal (u) axis until both curves overlap. This transformation takes the form $V_{\mathrm{PD}}(Ru + \Delta z_0) = V_{\mathrm{ref}}(z)$ and directly yields both R and Δz_0, the change in equilibrium position between the new data and reference data. If the uncalibrated data displays a significant portion of an interference fringe, it is said to be in the intermediate-amplitude regime ($\lambda/8 \lesssim R < \lambda/4$). In this case, shifting and scaling along the vertical (voltage) axis is also permitted, which allows some tolerance for slight changes in laser power or optical alignment. To determine whether the data is in the intermediate-amplitude regime, $V_{\mathrm{PD}}(u)$ is tested for linearity by fitting to a third-order polynomial. If either the quadratic or cubic coefficients exceed a predetermined fraction of the linear coefficient (in absolute value), the data is of intermediate amplitude. For most measurements, we use a 50% threshold.

Given that we use the widths of optical fringes in $V_{\mathrm{PD}}(u)$ as our primary means of calibrating distances, the question arises as to how consistent these fringe widths are within a single data set. Figures 3(e) and 3(f) demonstrate this consistency in uncalibrated data with 7 fringes, measured using the silicon nitride cantilever. These results are typical of our measurements and reveal a monotonic trend in the fringe width across the range of u (and therefore z) values. This monotonic behavior is not altogether surprising, as $V_{\mathrm{PD}}(u)$ is far from an ideal interference pattern with perfectly periodic fringes. From the left-most fringe to the right-most fringe, the data shows an overall change of $\approx 10\%$ in fringe width Δu, suggesting that our deflection estimates R can vary by

$\approx 10\%$ depending on which fringe is chosen as a reference for $\lambda/2$. We emphasize that any error this causes in our estimation of R is identical between measurements, and can be considered as a linear scaling factor. Although the measured R may differ from its true value by $\approx 10\%$, repeated R measurements can have a standard deviation better than $\approx 0.01\%$, as evidenced by the low noise level in Fig. 1(c). Therefore, changes in R and z_0 can still be discerned with high precision.

In the peak-to-peak method, peaks are first located roughly by finding $V_{\mathrm{PD}}(u)$ data points that correspond to local maxima with prominence above the noise level, followed by fine tuning using a quadratic fit in the neighborhood of each peak. These quadratic fits provide the peak locations and uncertainties, from which the uncertainty in Δu, R, and Δz_0 are calculated by error propagation. In the stretch method, we implement a least-squares minimization routine to numerically align the uncalibrated data $V_{\mathrm{PD}}(u)$ to the reference data $V_{\mathrm{ref}}(z)$. Linear interpolation is used to compare these two data sets along the same data points in z. If the uncalibrated data partially extends past the edges of the reference data, only data points in the overlapping region are used in the sum of squared residuals. The sum is then normalized by P^2, where P is the number of overlapping data points. Uncertainties in R and Δz_0 are then evaluated by adding small perturbations to the best-fit parameters, and thereby estimating the Jacobian matrix and covariance matrix of the system.

IV. VALIDITY OF THE MODEL

A key concern that must be addressed is whether the assumption of sinusoidal motion (in Eqs. (1) and (2)) accurately describes MEMS/NEMS behavior. This is especially important because the large vibration amplitudes needed to span interference fringes are likely to induce mechanical nonlinearities, such as nonlinear restoring forces. The equation of motion for an inertially-driven, damped mechanical resonator with nonlinear stiffening is given by:

$$\frac{d^2z}{dt^2} + \frac{2\pi f_0}{Q}\frac{dz}{dt} + (2\pi f_0)^2 z + \alpha_2 z^2 + \alpha_3 z^3 = -(2\pi f)^2 Z_b \cos(2\pi f t). \tag{3}$$

Here f_0 is the undamped resonant frequency, Q is the quality factor, α_2 and α_3 are the nonlinear coefficients, f is the drive frequency, Z_b is the vibration amplitude of the resonator's base, and z is the relative motion between the resonator and its base. For simplicity, mechanical losses are modeled by dz/dt viscous damping; however, approximations made in the derivation that follows ($Q \gg 1$, $f \approx f_0$) ensure that our results are generalizable to systems with other forms of damping, including internal friction. The equation above can be modified to describe a resonator driven by

an external force by substituting $-(2\pi f)^2 Z_b$ with F/m, where F is the force amplitude and m is the resonator mass. A derivation of this equation is provided in the Supplemental Sec. S3.

While most previous work focuses solely on a cubic restoring force, we have also included a z^2 force for increased generality. This even-exponent term breaks the symmetry between positive and negative deflections of z, which means that the resonator may experience a stronger restoring force when it is deflected up rather than down. In our cantilevers, this could be caused by the asymmetric clamping conditions at the cantilever base (sacrificial layer below and free space above) or by a vertical stress gradient within the cantilever from fabrication.

While Eq. (3) cannot be solved exactly, a solution can be obtained to arbitrary precision using perturbation theory[41,42]. The key results are presented below, but a full derivation is provided in the Supplemental Secs. S4 and S5. The derivation assumes that the MEMS/NEMS resonator has $Q \gg 1$, weak drive forces, and a drive frequency near resonance, otherwise stated as $|f - f_0| \ll f_0$. All these assumptions are consistent with typical MEMS/NEMS experiments. Under these conditions, the steady-state solution is

$$z(t) = z_0 + \sum_{n=1}^{\infty} R_n \cos(2\pi n f t + \theta_n) \tag{4}$$

where R_n and θ_n are the amplitude and phase of the n^{th} Fourier component of z. The validity of our calibration technique thus depends on the relative magnitudes of $R_2, R_3, \ldots, R_n$ to R_1. To lowest-order in perturbation theory, the first Fourier component is given by

$$R_1 = \frac{f_0 Z_b}{2\sqrt{(f - f_{\text{NL}})^2 + f_0^2/(2Q)^2}}, \tag{5}$$

where we have introduced the nonlinear resonant frequency, $f_{\text{NL}} = f_0 + \frac{3}{8}\alpha R_1^2 (4\pi^2 f_0)^{-1}$, and the combined nonlinear coefficient $\alpha = \alpha_3 - \frac{10}{9}\alpha_2^2 (2\pi f_0)^{-2}$. These equations for $R_1(f)$ and $f_{\text{NL}}(R_1)$ are plotted in Fig. 4. The function $f_{\text{NL}}(R_1)$ is often referred to as the 'backbone curve' of a nonlinear resonance peak. For a mechanical system with fixed f_0, Q, and α, the backbone curve follows the resonance peak maximum as the drive amplitude Z_b increases. The resonance peak $R_1(f)$ itself is symmetric for small drive amplitudes $Z_b \to 0$ or if $\alpha = 0$. For sufficiently large drive amplitudes (and $\alpha \neq 0$) the resonance peak leans asymmetrically to one side, eventually leading to a multi-valued region of $R_1(f)$. This causes hysteresis in experimental frequency sweeps as observed in Fig. 1(c). The resulting asymmetry can be characterized by the resonant frequency shift $\Delta f_0 = f_{\text{NL}} - f_0$, given by

$$\Delta f_0 = \frac{3\alpha R_1^2}{32\pi^2 f_0}. \tag{6}$$

The nonlinear resonator experiences a shift from its equilibrium position characterized by $z_0 \approx -\frac{1}{2}\alpha_2 R_1^2 (2\pi f_0)^{-2}$. This result shows that z_0 is due entirely to the symmetry breaking of the α_2 nonlinearity. Perturbation theory shows that the leading terms in the second and third Fourier components of $z(t)$ are given by:

$$\frac{R_2}{R_1} = \frac{1}{3}\frac{|z_0|}{R_1} \tag{7}$$

$$\frac{R_3}{R_1} = \left| \frac{1}{12}\frac{\Delta f_0}{f_0} + \frac{2}{9}\frac{|z_0|^2}{R_1^2} \right|. \tag{8}$$

Higher-order Fourier components R_n become exponentially smaller for increasing n based on the dimensionless ratios $|z_0|/R_1$ and $(\Delta f_0)/f_0$. Therefore, knowing these two ratios will allow us to determine whether higher-order components are negligible, as required by Eq. (1) in our optical calibration scheme.

V. RESULTS AND DISCUSSION

A. A Sample Frequency Sweep

To demonstrate the capabilities of our calibration scheme, Fig. 5 shows a Duffing resonance of the silicon nitride cantilever measured entirely in the time domain. The measurement was accomplished by collecting consecutive oscilloscope traces while sweeping the drive frequency upward from $f \approx 34.5\,\text{kHz}$ to $f \approx 35.2\,\text{kHz}$ with the laser spot focused near the cantilever free end. Oscilloscope data is shown at three stages of data processing in Fig. 5(a). First, raw data is mapped from the t domain to the u domain. Then, vibration amplitudes are extracted from the u-mapped data via the peak-to-peak method (for large amplitudes) or the stretch method (for small amplitudes). Multiplying the u axis by R allows us to plot the data versus displacement, since by definition $uR = z - z_0$. The calibrated data (Fig. 5(a) right panels) reveal nearly vertical optical fringes that maintain constant width as f varies. The slight tilt of these fringes away from vertical reveals the trend in z_0. The extracted values of R and z_0 are shown in Fig. 5(b). Since the choice of origin $z_0 = 0$ is arbitrary, here the value is chosen to correspond to the value far away from resonance.

We can now use Eqs. (7) and (8) to evaluate the validity of our model for u. Based on the results in Fig. 5(b), the maximum vibration amplitude is $R_1 \approx 1.75\,\lambda$; relative to a point far from

resonance this corresponds to an equilibrium shift $z_0 \approx 0.1\,\lambda$. Therefore, by Eq. (7), the second Fourier component of z has a maximum relative amplitude of $R_2/R_1 \approx 0.02$. If we estimate the intrinsic resonant frequency to be $f_0 \approx 34.7\,\text{kHz}$, the nonlinear frequency shift at maximum R_1 is $\Delta f_0 \approx 0.3\,\text{kHz}$. Thus, the third Fourier component has a maximum amplitude of $R_3/R_1 \approx 0.002$. With relative amplitudes of $\approx 2\%$ and $\approx 0.2\%$ for R_2 and R_3, respectively, we infer that R_1 alone is indeed sufficient to model the motion of z.

Figures 5(c) and 5(d) show measurements of the same cantilever under the same optical conditions, but while sweeping f under varying conditions. In Fig. 5(c), the same inertial drive voltage was used as in Fig. 5(a), but this time f was swept downward. Comparing these two results thus demonstrates how the hysteresis of the mechanical resonator affects the observed optical fringes. Similarly, Fig. 5(d) shows repeated upward sweeps of f, but for three different drive voltages. These plots reveal an increasing number of optical fringes as the Duffing resonance peak grows and becomes more asymmetric.

B. Spatial Mapping of MEMS/NEMS Motion

To demonstrate how the laser's lateral position on the MEMS/NEMS device can affect $V_{\text{PD}}(z)$, we have performed measurements while scanning the laser spot across a cantilever's long axis, x. This was accomplished by keeping the laser fixed while translating the cantilever laterally using motorized stages. The laser was a diode laser with $\lambda \approx 640\,\text{nm}$ and $1/e^2$ diameter $w \approx 4\,\mu\text{m}$. Figure 6 presents data for two different modes of cantilever motion. Position-dependent data was first taken while driving the fundamental mode with $f \approx 34.85\,\text{kHz}$ (Figs. 6(a)–6(c)), and then again while driving the second mode with $f \approx 217.7\,\text{kHz}$ (Figs. 6(d)–6(f)).

The transformed data (Figs. 6(a) and 6(d) middle panels) reveal nearly horizontal interference fringes due to a large static deflection of the cantilever. This upward deflection originated during device fabrication due to stress gradients in the LPCVD silicon nitride layer and can be seen in the electron micrograph of Fig. 1(a). The cantilever's large intrinsic deflection suggests a new method of extracting z_0 and R values based on counting optical fringes in vertical slices of the transformed data. Unlike horizontal data slices, which correspond to individual oscilloscope traces, vertical slices – shown in Figs. 6(b) and 6(e) – correspond to stroboscopic measurements of the cantilever during a fixed phase of its motion. Therefore, a vertical slice of Fig. 6(a) at $u = 0$ reveals the cantilever profile while it is at equilibrium $z(x) = z_0(x)$, and the vertical slices at $u = \pm 1$ reveal

the profiles at the extremes $z(x) = z_0(x) \pm R(x)$. Similar to an interference pattern from a single oscilloscope trace, each peak in this data is separated from its neighboring valleys by a distance of $\approx \lambda/4$. Therefore plotting the x coordinates of the local extrema, as is done in the Figs. 6(b) and 6(e) upper panels, reveals the deflection profile $z(x)$ of the cantilever. This is only possible if several fringes are traversed, as provided here by the cantilever's large intrinsic deflection.

Figures 6(c) and 6(f) show comparisons of R and z_0 obtained from horizontal slices (HS) and vertical slices (VS) of the transformed data for the two cantilever vibrational modes. For the fundamental mode, HS and VS provide nearly identical values for both z_0 and R, with deviations primarily near the cantilever base and free end. Within $\approx 2\,\mu$m of the cantilever free end, the HS peak-to-peak method shows a sudden downward trend in both R and z_0. This occurs as the incident laser steps off the cantilever, partially diffracting around the tip. This region is observable in Figs. 6(a) and 6(d) as a narrow band of distorted interference fringes around $x \approx 50\,\mu$m. Deviations between HS and VS methods near the cantilever base arise from small vibration amplitudes. Consequently, oscilloscope traces (horizontal slices) recorded bellow $x \lesssim 17\,\mu$m do not span a full $\lambda/2$ fringe, and must be compared using the stretch method. In comparison to the fixed-laser measurements of Fig. 5, the stretch method is inherently less reliable in these scanned-laser measurements because different cantilever coordinates x generally produce dissimilar interference patterns. These interference patterns may have differing fringe contrasts (peak or valley heights), due to the simple geometric effect that points nearer to the cantilever base must traverse a larger range of inclination angles to span the same vertical distance Δz. This is partially compensated by allowing vertical stretches when comparing interference patterns, but this extra degree of freedom is not available near the cantilever base where amplitudes are small and interference patterns are linear.

The accuracy of our HS and VS calibration methods can be assessed by comparing z_0 values to measurements from a commercial optical profilometer, also shown in Figs. 6(c) and 6(f). Our VS results, particularly near the cantilever base, are in better agreement with the optical profilometer than the HS results. The VS method and optical profilometry produce base-to-free-end deflections of $\Delta z_0 \approx 3.89\,\mu$m and $\Delta z_0 \approx 3.79\,\mu$m, respectively. Compared to our laser wavelength, this is a disagreement of $\approx 0.15\,\lambda$. However, as shown in Fig. 5(b) using the same cantilever and laser, a vibration amplitude of $R \approx 1.75\,\lambda$ (consistent with the free-end value in Fig. 6(c)) induces a static deflection of $\Delta z_0 \approx 0.1\,\lambda$. Accounting for this effect thus brings the disagreement between the VS method and optical profilometry down to $\approx 0.05\,\lambda$, or $\approx 30\,$nm.

When measuring the cantilever's second vibrational mode (Figs. 6(d)–6(f)), vibration amplitudes were not large enough to apply the HS peak-to-peak method. The VS method produced nearly identical z_0 values to those measured using the cantilever's fundamental mode, as well as a vibration profile $R(x)$ that closely matches expectations from Euler-Bernoulli beam theory. The HS stretch method yields unreliable results for both R and z_0 (Fig. 6(f)) due to the variations in cantilever inclination angle discussed earlier. This problem is highlighted by the vibrational node at $x \approx 39\,\mu$m, at which point our oscilloscope still measures a sinusoidal signal spanning roughly 25 mV due entirely to the time-varying cantilever angle.

C. Calibrating Lock-In Amplifier Measurements

As we have shown in the above sections, MEMS/NEMS interferometry measurements made in the time domain provide a direct means of extracting the system's interference pattern $V_{\mathrm{PD}}(z)$. While this technique is powerful, it is slower than more conventional lock-in amplifier (or spectrum analyzer) MEMS/NEMS measurements made in the frequency domain. This is because time-domain measurements, such as oscilloscope traces, require substantial averaging to achieve an acceptable signal-to-noise ratio. For instance, the frequency sweep shown in Fig. 5, which contains an oscilloscope trace for every f value, required 100 averages per oscilloscope trace, and thereby spanned ≈ 4 seconds per trace. A lock-in amplifier performing a similar measurement with a comparable voltage noise level would require a fraction of a second – albeit without providing the rich harmonic content seen in the oscilloscope traces. This disparity in noise level and averaging time is due to the high bandwidth ($\gtrsim 100$ MHz) that an oscilloscope requires to measure arbitrary waveforms. Such a high bandwidth permits far more noise into the measurement than the 1 Hz to 1 kHz operating bandwidths typical of lock-in amplifiers.

To understand the relationship between MEMS/NEMS interferometry measurements in the time and frequency domains, we must consider the Fourier transform of a typical time-dependent measurement $V_{\mathrm{PD}}(t)$ such as Fig. 3(a). Because the waveform has a period $T = f^{-1}$, it can be described by the Fourier series:

$$V_{\mathrm{PD}}(t) = V_0 + \sum_{n=1}^{\infty} V_n \cos\left(2\pi n f t + \phi_n\right). \tag{9}$$

Therefore, by measuring a sufficiently large number of the Fourier components V_n (and corresponding phases ϕ_n) with a lock-in amplifier, the waveform $V_{\mathrm{PD}}(t)$ can be approximately recon-

structed. To this end, we employ a digital lock-in amplifier capable of measuring eight distinct frequency bands simultaneously.

Figure 7 displays lock-in amplifier measurements of the silicon nitride cantilever and our approach to calibrating these measurements. These measurements were performed using a helium-neon laser with $\lambda \approx 633\,\text{nm}$ and $w \approx 7\,\mu\text{m}$. The lock-in amplifier provided the inertial drive signal at frequency f, and detected the resulting photodetector voltage at frequencies $f, 2f, \ldots, 8f$. In order to calibrate the lock-in data, a reference oscilloscope measurement $V_{\text{ref}}(t)$ was first performed and calibrated using the peak-to-peak method described in the previous sections. The resulting interference pattern $V_{\text{ref}}(z)$, shown in Fig. 7(a), was then used as a reference for all subsequent lock-in measurements. With this reference data, lock-in measurements were fitted to a numerical model to determine the mechanical parameters z_0 and R. This fit was performed by substituting into $V_{\text{ref}}(z)$ the expression $z(t) = z_0 + R\cos(2\pi f(t-t_0))$, and then numerically calculating the complex Fourier coefficients according to

$$\tilde{V}_n = \frac{1}{T}\int_0^T V_{\text{ref}}(z(t))\, e^{-i2\pi nt/T}\, dt. \tag{10}$$

These coefficients were compared to the lock-in measurements, expressed in phasor form as $V_n e^{i\phi_n}$, using a nonlinear least squares fit in which z_0 and R are the only free parameters. In these fits, the time of maximum deflection t_0 is determined from ϕ_1, the measured phase of the lowest Fourier component, as described below.

Lock-in data obtained at a fixed drive frequency $f \approx 35.01\,\text{kHz}$ is shown in Fig. 7(b), along with fit results based on $V_{\text{ref}}(z)$ and Eq. (10). The eight frequency components were measured in parallel, each with a bandwidth of $\approx 2\,\text{Hz}$. All lock-in amplitudes are reported in peak voltages. A fit is generated using the numerical model described above and yields values of $z_0/\lambda = 0.023 \pm 0.004$ and $R/\lambda = 1.997 \pm 0.004$, where the fit uncertainties signify one standard deviation. Also shown in Fig. 7(b) are the simulated time-trace $V_{\text{ref}}(z(t))$ based on this fit and a polar plot of the lock-in data after rotating each phasor $V_n e^{i\phi_n}$ by $-n\phi_1$. Such a rotation is equivalent to shifting the t axis in Eq. (9) by an amount $\Delta t = -\phi_1/(2\pi f)$. The plot of rotated data in Fig. 7(b) shows that all Fourier components V_n lie along the horizontal axis. This implies that the Fourier series given by Eq. (9) reduces to a Fourier cosine series, which has even symmetry at $t = 0$. Therefore, Δt defines one of the turning points $t_{\text{TP}} = t_0 + \frac{1}{2}NT$ described in Sec. III. In order to unambiguously determine t_0 and perform the fits described by Eq. (10), two separate fits were performed: one assuming $t_0 = \Delta t$, and another assuming $t_0 = \Delta t + \frac{1}{2}T$. With R constrained to positive values, the better of

these two fits determined the "correct" value of t_0.

A complete frequency sweep through a resonance of the cantilever, as measured by the lock-in amplifier, is displayed in Fig. 7(c). Amplitudes for the lowest Fourier component, V_1, bear some resemblance to a Duffing resonance, with a sudden drop at $f \approx 35.07\,\mathrm{kHz}$ suggestive of a right-leaning frequency peak, but with vertical undulations caused by the optical transduction. MEMS/NEMS motion is so large throughout this sweep that all of the measured Fourier components, from V_2 to V_8, are significantly larger than the RMS voltage noise level ($\approx 2\,\mu\mathrm{V}$) and display similar vertical trends to V_1, indicating motion much larger than $\lambda/2$. At each drive frequency a numerical fit of the eight Fourier components was conducted similar to that shown in Fig. 7(b) to determine z_0 and R. In this case, z_0 represents the shift in equilibrium position relative to $V_{\mathrm{ref}}(z)$. The mechanical parameters arising from these fits are shown in Fig. 7(d). As suspected, the vibration amplitudes R reveal a right-leaning Duffing peak.

In an effort to determine how many Fourier components must be measured to accurately determine R and z_0, we have repeated the fitting procedure for this frequency sweep using various subsets of the data. Because there are two free fit parameters, at least two Fourier components are needed. Figure 7(d) reveals that fits using only V_1 and V_2 are highly erratic, while those that use three or four Fourier components do not differ greatly from fits using all eight components. For each subset of data, the first fit was performed at $f \approx 35.07\,\mathrm{kHz}$, where the largest amplitude was expected, with guess parameters of $R/\lambda = 2.1$ and $z_0/\lambda = 0$. Subsequent fits used guess parameters based on the fit result at the previous drive frequency, with R/λ and z_0/λ values constrained within windows of width 0.5 and 0.1, respectively. To ensure that the fit routine did not settle on a false optimum, multiple fits were performed with guess R and z_0 values distributed evenly within these windows. In the range of $f \approx 34.6\,\mathrm{kHz}$ to $f \approx 35.07\,\mathrm{kHz}$, where the uncertainties in the fits were largest, the typical uncertainty in z_0/λ for the different data subsets (in order of 2, 3, 4, and 8 Fourier components) were approximately 0.2, 0.005, 0.004, and 0.003. These uncertainties were derived from the covariance matrix of each fit. The mean uncertainties in R were nearly identical to those in z_0.

A downward sweep of the drive frequency was also performed with this cantilever, mapping the lower branch of the hysteretic Duffing response. Measurements of V_1 and the fitted R values were presented in Figs. 1(b) and 1(c) as examples of MEMS/NEMS interferometry measurements. Here, all eight Fourier components were used for data fitting.

The calibration scheme presented in this section assumes that the interference pattern $V_{\mathrm{PD}}(z)$

remains constant between lock-in measurements. This assumes that the laser power and alignment of the entire optical system remains constant throughout the experiment, beginning with the reference oscilloscope trace. Furthermore, this calibration technique is only helpful if the MEMS/NEMS deflection z remains within the range spanned by $V_{\mathrm{ref}}(z)$. Hence, the oscilloscope trace should be recorded using a MEMS/NEMS vibration amplitude at least as large as the largest amplitude in the lock-in measurements.

D. Measurements of Silicon Cantilevers

To demonstrate the general applicability of our technique regardless of MEMS/NEMS materials and dimensions, Supplemental Sec. S1 provides measurements of two monolithic, single-crystal silicon cantilevers. The first of these has dimensions (length×width×thickness) of $\approx 50\,\mu\mathrm{m} \times 10\,\mu\mathrm{m} \times 250\,\mathrm{nm}$, roughly matching the silicon nitride cantilever presented in this main text. However, the dynamics of these two materials differ greatly as a result of silicon's optical absorption. The silicon cantilever absorbs $\approx 10\%$ of impinging laser power[43], leading to photothermal feedback[31,32,44] and self-oscillation[31,45–48] of the cantilever. We investigated this behavior through lock-in amplifier and oscilloscope measurements and present vibration profiles, $R(x)$, measured with and without self-oscillation.

The second silicon cantilever studied in Supplemental Sec. S1 has a similar length and thickness to the first, but a width of $\approx 2.5\,\mu\mathrm{m}$. This is substantially smaller than the laser spot diameter of $w \approx 7\,\mu\mathrm{m}$. The cantilever-substrate gap is $h \approx 2\,\mu\mathrm{m}$, leaving room for optical diffraction to influence our measurements. Despite this, a scanned-laser measurement reveals a vibration profile $R(x)$ and equilibrium profile $z_0(x)$ closely matching results for the wider silicon cantilever.

VI. CONCLUSION

We have demonstrated a general procedure for calibrating distances in laser interferometry measurements of MEMS/NEMS motion. This procedure is devised primarily for interferometry systems that utilize the MEMS/NEMS substrate as a static reference mirror, and exploits large-amplitude MEMS/NEMS motion to observe a full interference fringe (length $\approx \lambda/2$). Unlike existing calibration methods, our approach is independent of device materials and geometry, and it makes no *a priori* assumptions of the system's interference pattern. For interferometry data

recorded in the time domain, the transformation we have described from time t to the dimensionless variable u provides a robust and succinct means to extract the interference pattern of a general MEMS/NEMS system. In addition to providing motion calibration, this transformation enables the observation of linear changes in MEMS/NEMS vibration amplitude and equilibrium position even when the optical transduction is extremely nonlinear. Using this technique allows access to larger vibration amplitudes than previously possible, which can translate to improved signal-to-noise ratios in applications such as sensing. We have briefly investigated the impact of optical diffraction on our technique using a MEMS device narrower than the probing laser spot and found that the trends in vibration amplitude and static deflection are nearly identical to those observed with wider cantilevers. This suggests that our technique may be compatible with MEMS/NEMS devices narrower than the laser wavelength, provided that sufficient interference or diffraction occur to yield power variations above the baseline photodetector noise.

SUPPLEMENTARY MATERIALS

The supplementary material includes further demonstrations of our calibration technique using experimental measurements of monolithic silicon cantilevers. It also includes a brief discussion regarding the impact of substrate surface roughness on interferometry, a mathematical derivation of the inertially driven MEMS/NEMS equation of motion, and a derivation of Eqs. 4–8 using perturbation theory.

ACKNOWLEDGMENTS

This work was performed in part at the Physical Measurement Laboratory (PML) and the Center for Nanoscale Science and Technology (CNST) at the National Institute of Standards and Technology (NIST). S. Krylov acknowledges support from the Henry and Dinah Krongold Chair of Microelectronics. R. De Alba and C. B. Wallin acknowledge support under the Cooperative Research Agreement between the University of Maryland and the National Institute of Standards and Technology Center for Nanoscale Science and Technology, Award 70NANB14H209, through the University of Maryland.

REFERENCES

[1]B. Ilic, Y. Yang, K. Aubin, R. Reichenbach, S. Krylov, and H. G. Craighead, "Enumeration of dna molecules bound to a nanomechanical oscillator," Nano Letters **5**, 925–929 (2005).

[2]M. Li, H. X. Tang, and M. L. Roukes, "Ultra-sensitive nems-based cantilevers for sensing, scanned probe and very high-frequency applications," Nature Nanotechnology **2**, 114 (2007).

[3]D. Garcia-Sanchez, K. Y. Fong, H. Bhaskaran, S. Lamoreaux, and H. X. Tang, "Casimir force and in situ surface potential measurements on nanomembranes," Physical Review Letters **109**, 027202 (2012).

[4]J. Chaste, A. Eichler, J. Moser, G. Ceballos, R. Rurali, and A. Bachtold, "A nanomechanical mass sensor with yoctogram resolution," Nature Nanotechnology **7**, 301 (2012).

[5]M. S. Hanay, S. Kelber, A. K. Naik, D. Chi, S. Hentz, E. C. Bullard, E. Colinet, L. Duraffourg, and M. L. Roukes, "Single-protein nanomechanical mass spectrometry in real time," Nature Nanotechnology **7**, 602 (2012).

[6]E. Gavartin, P. Verlot, and T. J. Kippenberg, "A hybrid on-chip optomechanical transducer for ultrasensitive force measurements," Nature Nanotechnology **7**, 509 (2012).

[7]I. Mahboob and H. Yamaguchi, "Bit storage and bit flip operations in an electromechanical oscillator," Nature Nanotechnology **3**, 275 (2008).

[8]I. Mahboob, M. Mounaix, K. Nishiguchi, A. Fujiwara, and H. Yamaguchi, "A multimode electromechanical parametric resonator array," Scientific Reports **4**, 4448 (2014).

[9]R. B. Karabalin, R. Lifshitz, M. C. Cross, M. H. Matheny, S. C. Masmanidis, and M. L. Roukes, "Signal amplification by sensitive control of bifurcation topology," Physical Review Letters **106**, 094102 (2011).

[10]X. Zhou, F. Hocke, A. Schliesser, A. Marx, H. Huebl, R. Gross, and T. J. Kippenberg, "Slowing, advancing and switching of microwave signals using circuit nanoelectromechanics," Nature Physics **9**, 179 (2013).

[11]C. Chen, D. H. Zanette, J. R. Guest, D. A. Czaplewski, and D. López, "Self-sustained micromechanical oscillator with linear feedback," Physical Review Letters **117**, 017203 (2016).

[12]X. Li, T. Ono, Y. Wang, and M. Esashi, "Ultrathin single-crystalline-silicon cantilever resonators: Fabrication technology and significant specimen size effect on young's modulus," Applied Physics Letters **83**, 3081–3083 (2003).

[13]B. Ilic, S. Krylov, and H. G. Craighead, "Young's modulus and density measurements of thin atomic layer deposited films using resonant nanomechanics," Journal of Applied Physics **108**, 044317 (2010).

[14]R. De Alba, T. S. Abhilash, A. Hui, I. R. Storch, H. G. Craighead, and J. M. Parpia, "Temperature-dependence of stress and elasticity in wet-transferred graphene membranes," Journal of Applied Physics **123**, 095109 (2018).

[15]A. D. O'Connell, M. Hofheinz, M. Ansmann, R. C. Bialczak, M. Lenander, E. Lucero, M. Neeley, D. Sank, H. Wang, M. Weides, J. Wenner, J. M. Martinis, and A. N. Cleland, "Quantum ground state and single-phonon control of a mechanical resonator," Nature **464**, 697 (2010).

[16]T. P. Purdy, K. E. Grutter, K. Srinivasan, and J. M. Taylor, "Quantum correlations from a room-temperature optomechanical cavity," Science **356**, 1265 (2017).

[17]K. C. Balram, M. I. Davanço, J. D. Song, and K. Srinivasan, "Coherent coupling between radiofrequency, optical and acoustic waves in piezo-optomechanical circuits," Nature Photonics **10**, 346 (2016).

[18]Q. Li, M. Davanço, and K. Srinivasan, "Efficient and low-noise single-photon-level frequency conversion interfaces using silicon nanophotonics," Nature Photonics **10**, 406 (2016).

[19]B. J. Roxworthy and V. A. Aksyuk, "Nanomechanical motion transduction with a scalable localized gap plasmon architecture," Nature Communications **7**, 13746 (2016).

[20]A. Eichler, J. Chaste, J. Moser, and A. Bachtold, "Parametric amplification and self-oscillation in a nanotube mechanical resonator," Nano Letters **11**, 2699–2703 (2011).

[21]J. S. Bunch, A. M. van der Zande, S. S. Verbridge, I. W. Frank, D. M. Tanenbaum, J. M. Parpia, H. G. Craighead, and P. L. McEuen, "Electromechanical resonators from graphene sheets," Science **315**, 490 (2007).

[22]V. Singh, S. J. Bosman, B. H. Schneider, Y. M. Blanter, A. Castellanos-Gomez, and G. A. Steele, "Optomechanical coupling between a multilayer graphene mechanical resonator and a superconducting microwave cavity," Nature Nanotechnology **9**, 820 (2014).

[23]J. Lee, Z. Wang, K. He, J. Shan, and P. X. L. Feng, "High frequency mos2 nanomechanical resonators," ACS Nano **7**, 6086–6091 (2013).

[24]Z. Wang, H. Jia, X. Zheng, R. Yang, Z. Wang, G. J. Ye, X. H. Chen, J. Shan, and P. X. L. Feng, "Black phosphorus nanoelectromechanical resonators vibrating at very high frequencies," Nanoscale **7**, 877–884 (2015).

[25]N. Morell, A. Reserbat-Plantey, I. Tsioutsios, K. G. Schädler, F. Dubin, F. H. L. Koppens, and A. Bachtold, "High quality factor mechanical resonators based on wse2 monolayers," Nano Letters **16**, 5102–5108 (2016).

[26]X.-Q. Zheng, J. Lee, and P. X. L. Feng, "Hexagonal boron nitride nanomechanical resonators with spatially visualized motion," Microsystems & Nanoengineering **3**, 17038 (2017).

[27]D. W. Carr and H. G. Craighead, "Fabrication of nanoelectromechanical systems in single crystal silicon using silicon on insulator substrates and electron beam lithography," Journal of Vacuum Science & Technology B **15**, 2760–2763 (1997).

[28]B. Ilic, S. Krylov, K. Aubin, R. Reichenbach, and H. G. Craighead, "Optical excitation of nanoelectromechanical oscillators," Applied Physics Letters **86**, 193114 (2005).

[29]R. B. Karabalin, M. H. Matheny, X. L. Feng, E. Defaÿ, G. Le Rhun, C. Marcoux, S. Hentz, P. Andreucci, and M. L. Roukes, "Piezoelectric nanoelectromechanical resonators based on aluminum nitride thin films," Applied Physics Letters **95**, 103111 (2009).

[30]Z. Wang, J. Lee, and P. X. L. Feng, "Spatial mapping of multimode brownian motions in high-frequency silicon carbide microdisk resonators," Nature Communications **5**, 5158 (2014).

[31]R. A. Barton, I. R. Storch, V. P. Adiga, R. Sakakibara, B. R. Cipriany, B. Ilic, S. P. Wang, P. Ong, P. L. McEuen, J. M. Parpia, and H. G. Craighead, "Photothermal self-oscillation and laser cooling of graphene optomechanical systems," Nano Letters **12**, 4681–4686 (2012).

[32]R. De Alba, T. S. Abhilash, R. H. Rand, H. G. Craighead, and J. M. Parpia, "Low-power photothermal self-oscillation of bimetallic nanowires," Nano Letters **17**, 3995–4002 (2017).

[33]E. Gil-Santos, D. Ramos, J. Martínez, M. Fernández-Regúlez, R. García, Á. San Paulo, M. Calleja, and J. Tamayo, "Nanomechanical mass sensing and stiffness spectrometry based on two-dimensional vibrations of resonant nanowires," Nature Nanotechnology **5**, 641 (2010).

[34]D. Ramos, E. Gil-Santos, V. Pini, J. M. Llorens, M. Fernández-Regúlez, Á. San Paulo, M. Calleja, and J. Tamayo, "Optomechanics with silicon nanowires by harnessing confined electromagnetic modes," Nano Letters **12**, 932–937 (2012).

[35]D. Ramos, E. Gil-Santos, O. Malvar, J. M. Llorens, V. Pini, A. S. Paulo, M. Calleja, and J. Tamayo, "Silicon nanowires: where mechanics and optics meet at the nanoscale," Scientific Reports **3**, 3445 (2013).

[36]W. K. Hiebert, D. Vick, V. Sauer, and M. R. Freeman, "Optical interferometric displacement calibration and thermomechanical noise detection in bulk focused ion beam-fabricated nanoelectromechanical systems," Journal of Micromechanics and Microengineering **20**, 115038 (2010).

[37]M. V. Salapaka, H. S. Bergh, J. Lai, A. Majumdar, and E. McFarland, "Multi-mode noise analysis of cantilevers for scanning probe microscopy," Journal of Applied Physics **81**, 2480–2487 (1997).

[38]B. D. Hauer, C. Doolin, K. S. D. Beach, and J. P. Davis, "A general procedure for thermomechanical calibration of nano/micro-mechanical resonators," Annals of Physics **339**, 181–207 (2013).

[39]R. J. Dolleman, D. Davidovikj, H. S. J. van der Zant, and P. G. Steeneken, "Amplitude calibration of 2d mechanical resonators by nonlinear optical transduction," Applied Physics Letters **111**, 253104 (2017).

[40]D. Karabacak, T. Kouh, and K. L. Ekinci, "Analysis of optical interferometric displacement detection in nanoelectromechanical systems," Journal of Applied Physics **98**, 124309 (2005).

[41]A. H. Nayfeh and D. T. Mook, *Nonlinear Oscillations* (Wiley-VCH, 1995).

[42]R. H. Rand, "Lecture notes on nonlinear vibrations," (2012), PDF document retrieved from Cornell eCommons website: https://hdl.handle.net/1813/28989.

[43]D. E. Aspnes and A. A. Studna, "Dielectric functions and optical parameters of si, ge, gap, gaas, gasb, inp, inas, and insb from 1.5 to 6.0 ev," Physical Review B **27**, 985–1009 (1983).

[44]C. H. Metzger and K. Karrai, "Cavity cooling of a microlever," Nature **432**, 1002 (2004).

[45]M. Zalalutdinov, K. L. Aubin, M. Pandey, A. T. Zehnder, R. H. Rand, H. G. Craighead, J. M. Parpia, and B. H. Houston, "Frequency entrainment for micromechanical oscillator," Applied Physics Letters **83**, 3281–3283 (2003).

[46]K. Aubin, M. Zalalutdinov, T. Alan, R. B. Reichenbach, R. Rand, A. Zehnder, J. Parpia, and H. Craighead, "Limit cycle oscillations in cw laser-driven nems," Journal of Microelectromechanical Systems **13**, 1018–1026 (2004).

[47]M. Pandey, K. Aubin, M. Zalalutdinov, R. B. Reichenbach, A. T. Zehnder, R. H. Rand, and H. G. Craighead, "Analysis of frequency locking in optically driven mems resonators," Journal of Microelectromechanical Systems **15**, 1546–1554 (2006).

[48]D. B. Blocher, A. T. Zehnder, and R. H. Rand, "Entrainment of micromechanical limit cycle oscillators in the presence of frequency instability," Journal of Microelectromechanical Systems **22**, 835–845 (2013).

FIGURES

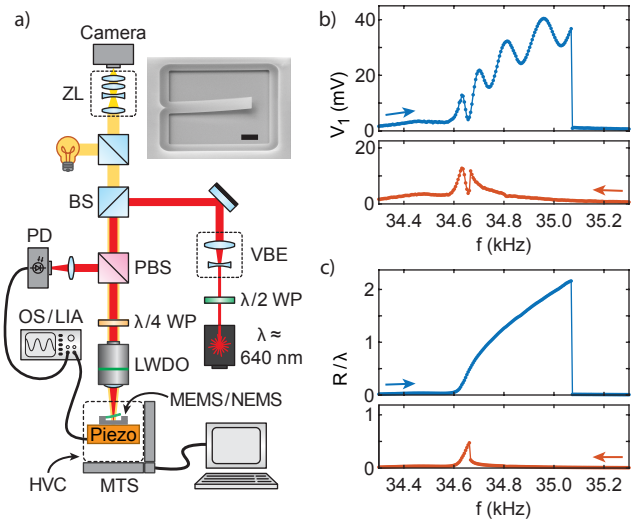

FIG. 1. The experimental setup and typical measurements. (a) Schematic of the experimental setup. The system consists of a laser source ($\lambda \approx 640\,\text{nm}$), a long-working-distance objective (LWDO), a 50/50 beam splitter (BS), a polarizing beam splitter (PBS), a high-speed photodetector (PD), waveplates (WP), a variable beam expander (VBE), a zoom lens (ZL), a camera, motorized translation stages (MTS), a high-vacuum chamber (HVC), a lock-in ampplifier (LIA), and an oscilloscope (OS). Inset: tilted view electron micrograph of the $\approx 50\,\mu$m-long silicon nitride cantilever used in our experiments. The scale bar is $\approx 10\,\mu$m. (b) Optically measured response of the cantilever to inertial forcing near its resonant frequency. As the drive frequency, f, is swept upward (top) or downward (bottom), a lock-in amplifier measures the response amplitude, V_1, in a narrow frequency band around f. Based on repeated sweeps, the noise level is $\approx 100\,\mu$V, which is smaller than the marker size. The prominent undulations are artifacts of the nonlinear optical readout; the dependence on sweep direction is due to a mechanical (Duffing) nonlinearity of the cantilever. (c) Cantilever vibration amplitudes, R, extracted from the data in (b) and from additional data (shown in Fig. 7), as described in Sec. V C. In this view, the data reveals a well understood Duffing resonance.

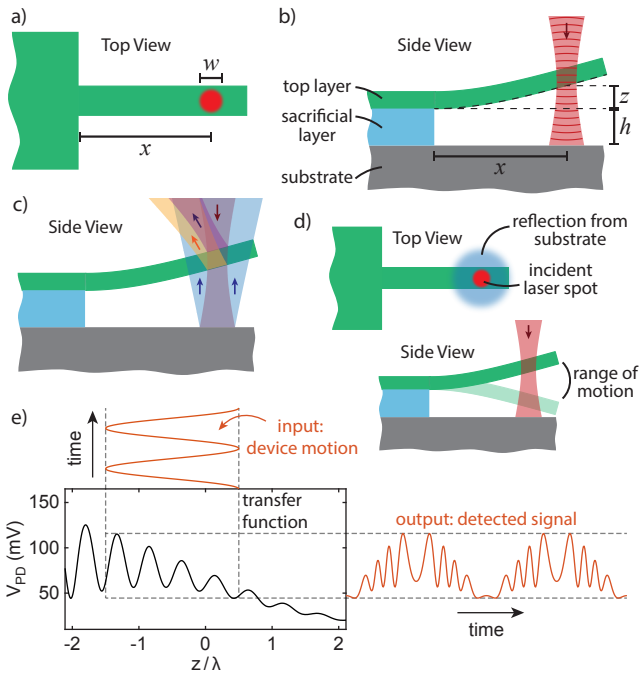

FIG. 2. Origin of the interference pattern and its influence on measurements. (a)–(d) Cartoon schematics of laser interferometry using a MEMS/NEMS cantilever. (a) and (b) An incident Gaussian beam is focused near the cantilever tip at lateral position x. The laser beam has a focused spot diameter w, and diverges on length scales comparable to h, the sacrificial layer thickness. (c) Reflections are generated at each optical interface. Reflected light may be off-axis with the original laser beam, complicating the total power collected by the photodetector. (d) Other optical non-idealities: Differing laser spot sizes in the device plane (top panel) and the changing device angle during motion (bottom panel). (e) Main panel: A sample interference pattern measured using a silicon nitride cantilever. Projections upward and rightward demonstrate the action of this interference pattern, $V_{\mathrm{PD}}(z)$, as a transfer function that relates the input device motion, $z(t)$, to the output detected signal, $V_{\mathrm{PD}}(t)$. In this example, the motion is centered about $z_0 = -0.5\,\lambda$ with amplitude $R = 1.0\,\lambda$.

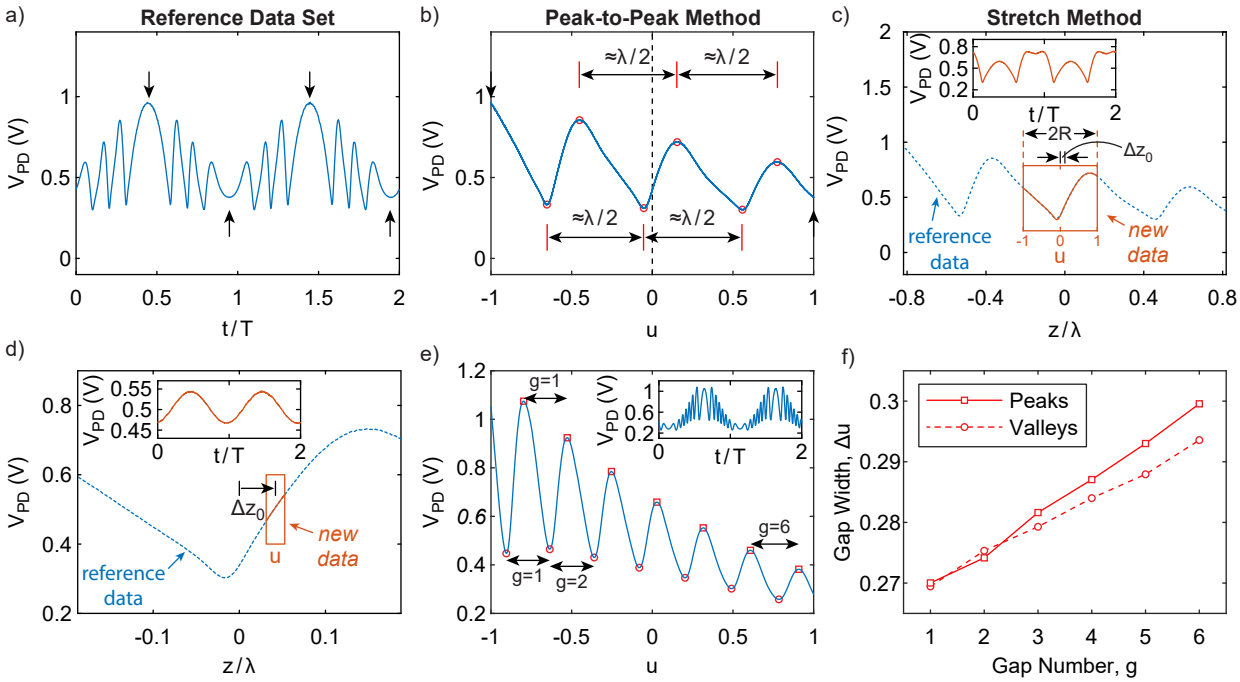
a)
Reference Data Set
V_{PD} (V)
t/T
b)
Peak-to-Peak Method
≈λ/2
≈λ/2
≈λ/2
≈λ/2
V_{PD} (V)
u
c)
Stretch Method
V_{PD} (V)
t/T
2R
Δz_0
reference data
new data
u
z/λ
d)
V_{PD} (V)
t/T
Δz_0
u
new data
reference data
z/λ
e)
g=1
g=1
g=2
g=6
V_{PD} (V)
t/T
u
f)
Peaks
Valleys
Gap Width, Δu
Gap Number, g

FIG. 3. Motion calibration using time-domain measurements of a silicon nitride cantilever. (a) An oscilloscope trace of large-amplitude MEMS/NEMS motion, $R > \lambda/4$. Data shown has been averaged from a longer oscilloscope trace consisting of 10 periods of oscillation. Based on variations between the measured periods, the noise level is $\approx 3\,\mathrm{mV}$. Arrows indicate points of even symmetry, corresponding to extremes of motion; these map to $u = \pm 1$. (b) The same data as (a), after mapping time t to normalized deflection u (see Eq. (2)). This plot contains four overlapping, nearly indistinguishable curves, because (a) spans two full periods of motion. Vertical arrows correspond to the symmetry points noted in (a). Neighboring pairs of peaks or valleys (marked with open circles) are separated by gaps of width $\approx \lambda/2$ that serve as reference lengths. We refer to this as the peak-to-peak method of calibration. Movement of one particular peak along the u axis can be monitored between measurements to track changes in z_0, the static deflection. (c) For smaller MEMS/NEMS motion ($R < \lambda/4$), a pre-calibrated data set (dashed curve) is used as reference. New data (solid red line and inset) is shifted and scaled until it overlaps with the reference data; we refer to this as the stretch method. Shifts and scaling along the u-axis provide the change in equilibrium position, Δz_0, and the vibration amplitude, R, respectively. If the new data displays a significant portion of an optical fringe, vertical adjustments are also permitted to allow some tolerance for changes in laser power or optical alignment. (d) For very-small-amplitude MEMS/NEMS motion ($R \ll \lambda/8$), the data appears sinusoidal in the time domain (inset) and linear in the u domain (solid red diagonal line); vertical adjustments are not permitted. (e) and (f) An example of the typical consistency of peak-to-peak and valley-to-valley gap widths in large-amplitude data. Inset in (e): Raw data before the $t \to u$ mapping.

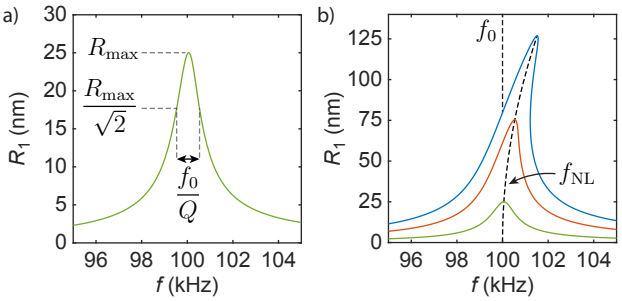

FIG. 4. Theoretical resonance peaks for a system with nonlinear stiffening, produced using Eq. (5). All curves assume parameter values of $f_0 = 100\,\mathrm{kHz}$, $Q = 100$, and $\alpha = 1\,\mathrm{kHz}^2 \cdot \mathrm{nm}^{-2}$; curves vary only in inertial drive amplitude Z_b. (a) A resonance peak in the linear regime, displaying the definition of the quality factor Q. The drive amplitude is $Z_b = 0.25\,\mathrm{nm}$. (b) Transition into the nonlinear regime. Solid curves, from bottom to top, have Z_b values of $0.25\,\mathrm{nm}$, $0.75\,\mathrm{nm}$, and $1.25\,\mathrm{nm}$. The nonlinear resonant frequency f_{NL} (dashed curve) is plotted as a function of R_1; this is often referred to as the "backbone curve".

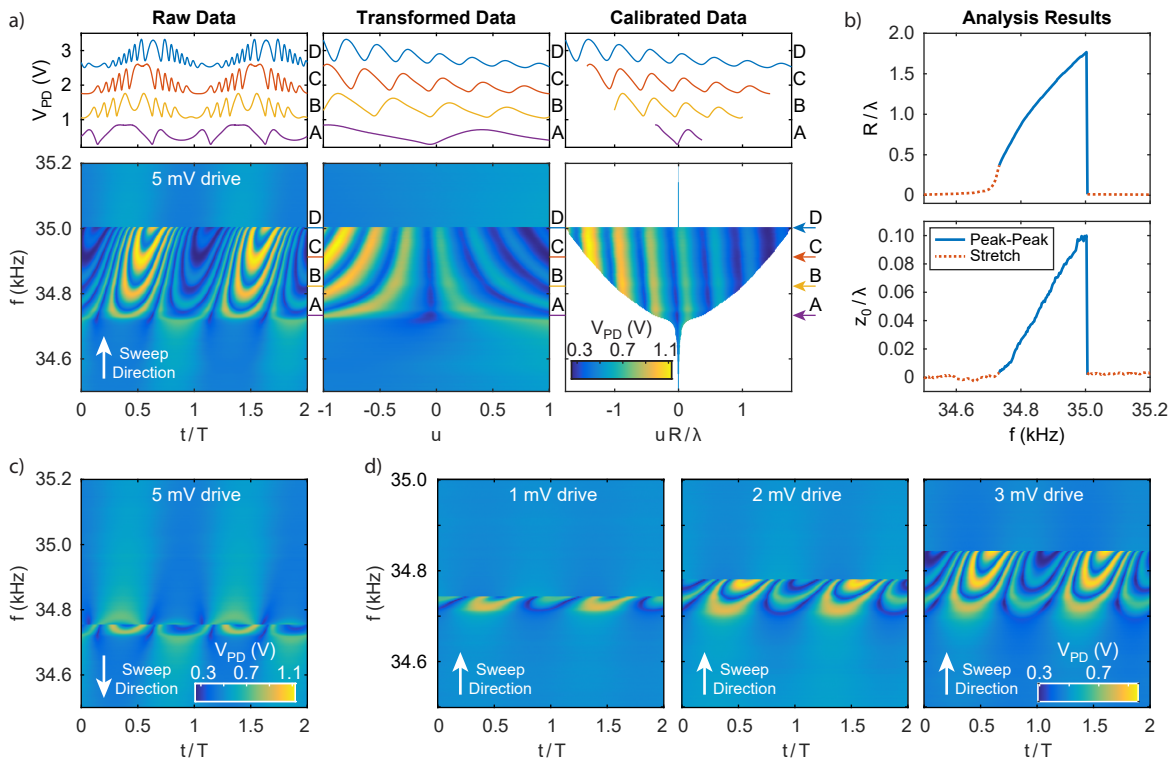

FIG. 5. Measurements of a Duffing resonance in a silicon nitride cantilever. All measurements were performed with the detection laser focused near the cantilever free end. (a) and (b) Data recorded during an incremental upward sweep of the drive frequency from $f \approx 34.5\,\mathrm{kHz}$ to $f \approx 35.2\,\mathrm{kHz}$ with a drive voltage of $\approx 5\,\mathrm{mV}$. (a) Oscilloscope data at several stages of data processing. Left panels: Raw oscilloscope data plotted versus normalized time, t/T, where $T = f^{-1}$. Middle panels: The same data after the $t \to u$ transformation. Right panels: The same data after calibration, plotted versus displacement $uR = z - z_0$. Upper panels display individual oscilloscope traces taken from the lower panels at the f values indicated by arrows A through D. Data in the upper panels are shifted vertically for clarity. Data in the lower panels use the same color scale. (b) The vibration amplitudes R and equilibrium positions z_0 obtained by applying the peak-to-peak and stretch calibration methods to the transformed data $V_{\mathrm{PD}}(u)$. Uncertainties in R and z_0 from these techniques are smaller than the line width. The evolving z_0 values can be seen in the bottom right panel of (a) as a slight tilt of the optical fringes away from vertical. (c) A downward frequency sweep using the same drive voltage as (a), showing hysteresis. (d) Upward frequency sweeps at drive voltages of approximately 1 mV, 2 mV, and 3 mV. All panels use the same color scale.

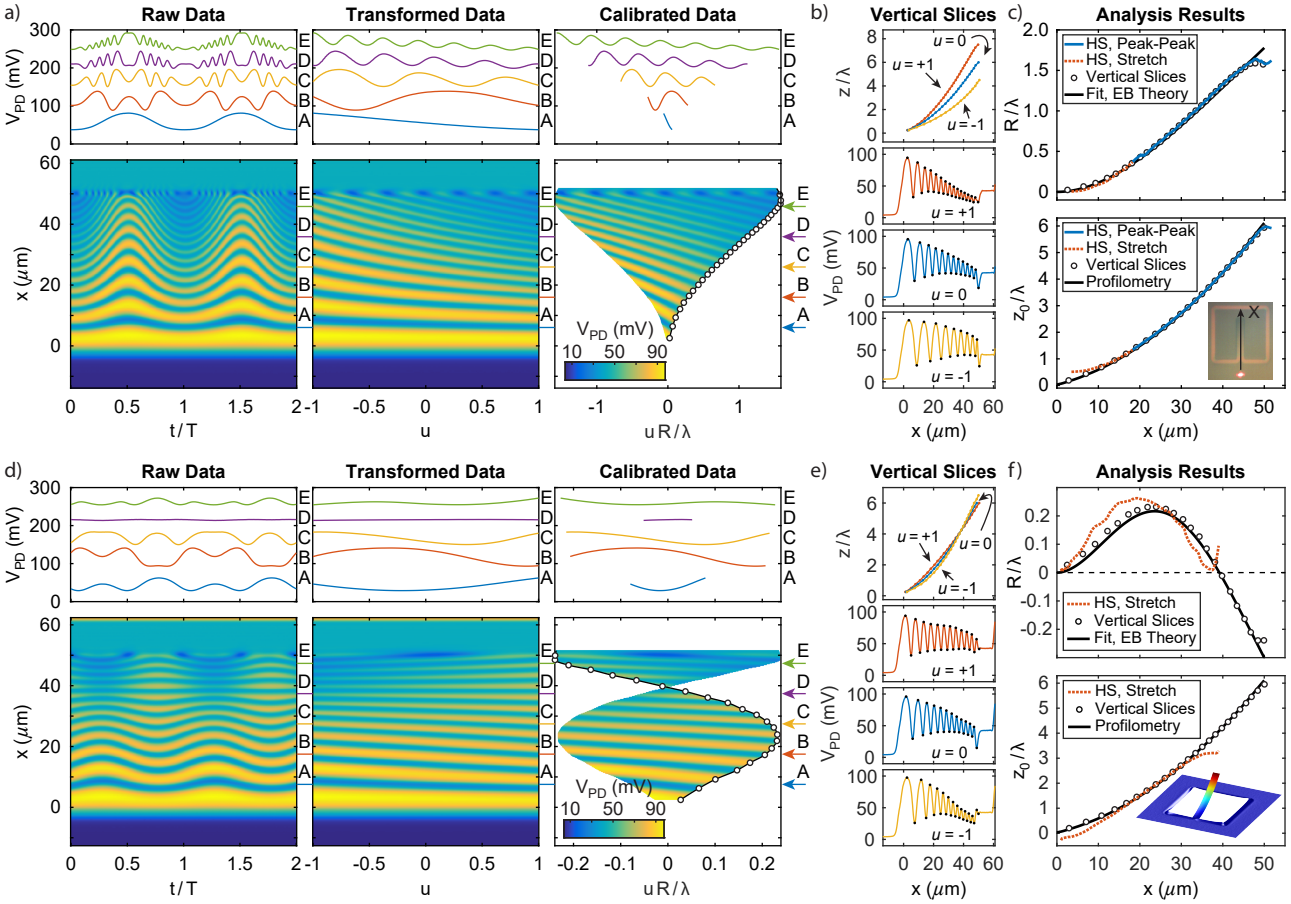
a)
Raw Data
Transformed Data
Calibrated Data
b)
Vertical Slices
c)
Analysis Results
HS, Peak-Peak
HS, Stretch
Vertical Slices
Fit, EB Theory
Profilometry
d)
e)
f)
t/T
u
uR/λ
x (μm)
z/λ
R/λ
z0/λ
VPD (mV)

FIG. 6. Spatial vibration mapping of a silicon nitride cantilever. (a)–(c) Data taken while exciting the fundamental cantilever mode with $f \approx 34.85\,\mathrm{kHz}$. (a) Left panels: Raw oscilloscope data recorded during an incremental upward sweep of the laser position, x, in steps of $\approx 0.25\,\mu\mathrm{m}$. The cantilever base and free end correspond to $x \approx 0\,\mu\mathrm{m}$ and $x \approx 50\,\mu\mathrm{m}$, respectively. Middle panels: The same data after the $t \to u$ transformation. Right panels: The same data after distance calibration using the vertical slices method. Upper panels display individual oscilloscope traces taken from the lower panels at the x coordinates indicated by arrows labeled A through E. Data in the upper panels are shifted vertically for clarity. Data in the lower panels use the same color scale. Open circles in the bottom right panel are the vibration amplitudes R determined using the vertical slices method. (b) Lower three panels: Vertical slices through the Transformed Data in (a) at $u = 0$ and $u = \pm 1$. Local extrema are marked by black points. Uppermost panel: Deflection profiles $z(x)$ obtained from the vertical slices by assuming local extrema are spaced every $\Delta z = \lambda/4$. These show the cantilever profile while it is at equilibrium ($u = 0$), and while it is at the outer limits of its motion ($u = \pm 1$). (c) Vibration amplitudes R and equilibrium positions z_0 extracted from (a), using the vertical slices method, horizontal slice (HS) peak-to-peak method, and HS stretch method. Vertical slices data use a 3 point moving average. Also shown are the static deflection measured by a commercial optical profilometer and a fit of the vibration profile to Euler-Bernoulli (EB) beam theory. Inset: The laser starting position as viewed by the camera in our setup. (d)–(f) Similar data to (a)–(c), but taken during excitation of the second cantilever mode with $f \approx 217.7\,\mathrm{kHz}$. Inset in (f): Optical profilometry image of the cantilever.

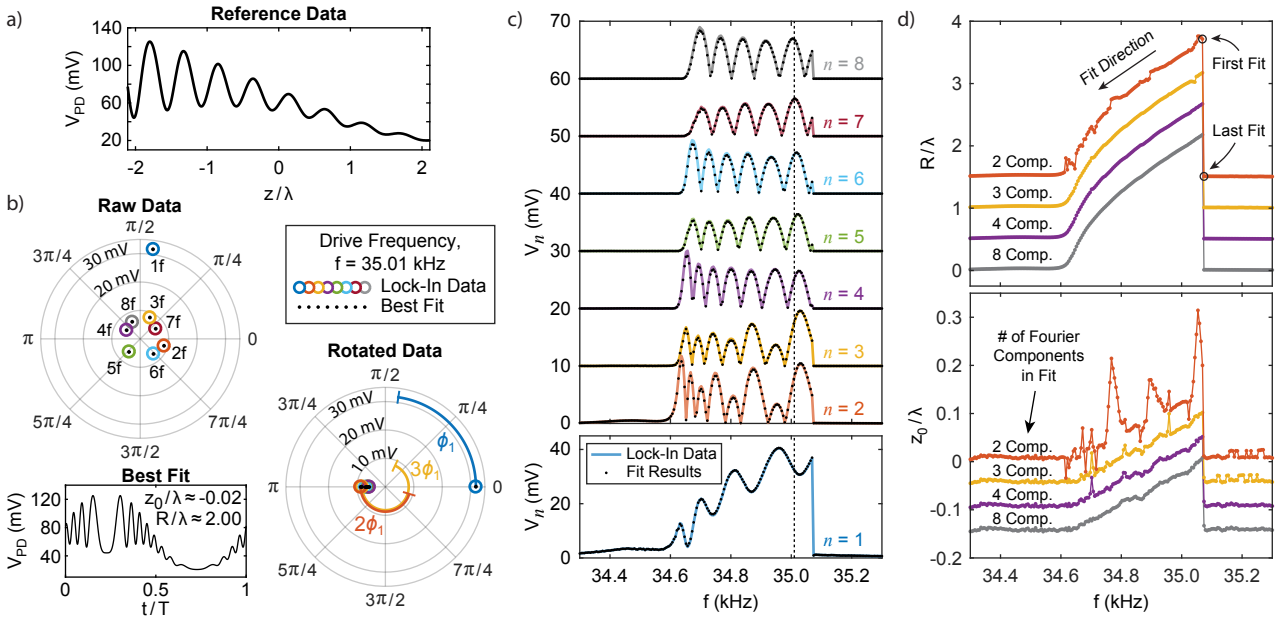
a)
Reference Data
V_{PD} (mV)
z / λ
b)
Raw Data
30 mV
20 mV
1f
2f
3f
4f
5f
6f
7f
8f
Drive Frequency,
f = 35.01 kHz
Lock-In Data
Best Fit
Rotated Data
10 mV
ϕ_1
$2\phi_1$
$3\phi_1$
Best Fit
$z_0/\lambda \approx -0.02$
$R/\lambda \approx 2.00$
t / T
c)
V_n (mV)
n = 8
n = 7
n = 6
n = 5
n = 4
n = 3
n = 2
n = 1
Lock-In Data
Fit Results
f (kHz)
d)
R / λ
Fit Direction
First Fit
Last Fit
2 Comp.
3 Comp.
4 Comp.
8 Comp.
z_0/λ
# of Fourier Components in Fit
f (kHz)

FIG. 7. Using an oscilloscope trace as a calibration tool for lock-in measurements. (a) The interference pattern of a silicon nitride cantilever, measured by an oscilloscope and calibrated using the peak-to-peak method. This curve, $V_{\mathrm{ref}}(z)$, is then used as a reference by which to calibrate lock-in measurements. (b) Upper left panel: Lock-in measurements recorded while driving the cantilever motion at $f \approx 35.01\,\mathrm{kHz}$. The lock-in measures the amplitudes V_n and phases ϕ_n of various Fourier components of the photodetector voltage at frequencies $f, 2f, \ldots, 8f$, shown as open circles. Black dots represent fit results based on the reference data in (a), as described by Eq. (10). Bottom left panel: a simulated time-trace $V_{\mathrm{ref}}(z(t))$ based on the fit results. Bottom right panel: the lock-in data, after rotating each Fourier component V_n by $-n\phi_1$. Perfect alignment along the horizontal axis proves that the photodetector voltage $V_{\mathrm{PD}}(t)$ has the even symmetry we expect at time $t_{\mathrm{TP}} = -\phi_1/(2\pi f)$, corresponding to a mechanical turning point. (c) A sweep of the drive frequency f, as measured by the lock-in amplifier at the eight frequencies $f, \ldots, 8f$, each with a bandwidth of $\approx 2\,\mathrm{Hz}$ (solid lines). The measurement error is smaller than the line width. Although only amplitudes V_n are shown, phases were also collected. For each f value, a fit is performed (black dots) using all eight Fourier components and the reference data in (a). A vertical dashed line denotes $f \approx 35.01\,\mathrm{kHz}$, from which the data in (b) is taken. (d) Mechanical parameters R and z_0 resulting from the fits in (c). For fitted values, error bars are comparable to or smaller than the marker size. The fits were repeated multiple times using different subsets of the data, from only the lowest two Fourier components to all eight components. Results are vertically offset for clarity, with the eight-component curves having no offset. In all cases, the first fit was performed at the f value indicated, and fits progressed in the direction indicated. Further details on the fitting procedure and the resulting uncertainties in R and z_0 are provided in the text.

Absolute Deflection Measurements in a Micro- and Nano-Electromechanical Fabry-Perot Interferometry System

Roberto De Alba,[1,2] Christopher B. Wallin,[1,2] Glenn Holland,[1] Slava Krylov,[3] and B. Robert Ilic[1,*]

[1]*Physical Measurement Laboratory, National Institute of Standards and Technology, Gaithersburg, MD 20899, USA*

[2]*Institute for Research in Electronics and Applied Physics, University of Maryland, College Park, MD 20742, USA*

[3]*School of Mechanical Engineering, Faculty of Engineering, Tel Aviv University, Ramat Aviv 69978, Tel Aviv, Israel*

CONTENTS

S1. MEASUREMENTS OF SILICON MEMS CANTILEVERS

In order to demonstrate the general applicability of our technique regardless of MEMS/NEMS materials and dimensions, we have performed measurements with single-crystal silicon cantilevers fabricated from a commercial silicon-on-insulator (SOI) wafer. Results from two such cantilevers are provided here. Section S1 A presents results for a $\approx 10\,\mu$m-wide cantilever, and Sec. S1 B presents results for a $\approx 2.5\,\mu$m-wide cantilever. In both cases, the cantilever lengths and thicknesses are $\approx 50\,\mu$m and $\approx 250\,$nm, respectively. All results were collected using a helium-neon laser with wavelength $\lambda \approx 633\,$nm and $1/e^2$ diameter $w \approx 7\,\mu$m at its focus. The cantilevers are separated from their silicon substrate by a gap of $\approx 2\,\mu$m.

Unlike the silicon nitride cantilever studied in the main text, which has negligible optical absorption throughout the visible spectrum [1], optical absorption in the crystalline silicon cantilevers studied here can greatly impact device mechanics. With an extinction coefficient of $k \approx 0.02$ at $\lambda \approx 633\,$nm, a 250 nm silicon layer absorbs roughly $(1 - \exp(-4\pi k\, 250/633)) \approx 9.4\%$ of incoming laser power [2]. This absorption can influence the dynamics of our resonators via the photothermal effect [3–5], which couples absorption to cantilever deflection via thermal expansion. This effect can cause feedback that amplifies or suppresses resonant motion depending on where the cantilever resides within the optical standing wave formed by the incident laser.

In this section, we demonstrate photothermal feedback in both of the silicon cantilevers under study. In both devices, the most striking consequence of this effect is entrained self-oscillation, i.e. synchronization between the photothermally-driven oscillations of the cantilever and the applied inertial drive [4, 6–9]. This is characterized by a flat amplitude-frequency relation over a range of drive frequencies near the cantilever resonance. This behavior is sustainable so long as the incident laser power and inertial drive strength are sufficiently high. The vibrational amplitude is self-limited by the laser wavelength in the sense that beyond a certain deflection the gain provided by photothermal feedback is no longer positive and amplification stops. With sufficient laser power the cantilever oscillates even in the absence of an inertial drive signal, with a frequency and phase randomly fluctuating near the resonance. With a drive signal applied, however, the cantilever oscillations become entrained to the drive frequency. All measurements shown in this section were per-

formed using $\approx 20\,\mu$W of incident laser power, with varying inertial drive strengths. This laser power was chosen as a compromise between adequate signal-to-noise ratio and modest photothermal effects. Because of the flat amplitude-frequency relation during entrainment, we will henceforth refer to the range of frequencies that exhibit entrainment as the 'flat-top.'

A. Measurements of a $\approx 10\,\mu$m wide cantilever

Measurements on the $\approx 10\,\mu$m-wide silicon cantilever are shown in Figs. S1–S5. Images of the cantilever and of the incident laser profile, as viewed by the camera in our experimental setup, are shown in Fig. S1(a). This cantilever demonstrated hysteresis during sweeps of the drive frequency, as shown in Figs. S1(b)–S1(d). The flat-top response was observed only during down-sweeps of the drive frequency, over a frequency range determined by the drive strength. The flat-top itself, which ordinarily resembles a rectangle function when plotted as amplitude versus frequency, is obscured by the nonlinear optical transduction. However, the flat amplitude response is easily distinguishable as a narrow frequency range in which all of the measured lock-in harmonics, i.e. the Fourier components of the photodetector voltage, have constant amplitude.

Figures S2 and S3 display measurements taken while scanning the laser along the cantilever length and across its width. In both cases a drive frequency of $f \approx 124.2\,$kHz was applied. This is outside the flat-top region and was intended to provide data of linear cantilever behavior in which photothermal effects are minimal. Diffraction effects occur as the laser approaches cantilever edges, distorting the measured z_0 values near $x \approx 50\,\mu$m in Fig. S2(c) and $y \approx \pm 5\,\mu$m in Fig. S3(c). The vibration amplitudes in Fig. S2(c) are roughly consistent with an Euler-Bernoulli fundamental mode, with peak amplitudes that increase approximately linearly with increasing drive strength. R values measured across the cantilever width (Fig. S3(c)) are roughly constant despite laser diffraction at the cantilever edges. The oscilloscope traces showed sufficient signal-to-noise ratios and fringe contrast to provide R measurements even at $y \approx \pm 8.5\,\mu$m, which corresponds to a laser spot centered $\approx 3.5\,\mu$m off of the cantilever. This distance corresponds to $w/2$, i.e. the laser spot radius. The R values measured within the entire measurable range of $y \approx -8.5\,\mu$m to $y \approx 8.5\,\mu$m have an arithmetic mean and standard deviation of $R = (0.97 \pm 0.01)\lambda$. In the raw data shown in Figs. S2(d) and S3(d), decreasing drive strength results in lower vibration am-

plitudes which is immediately discernable as a decrease in the number of observed optical fringes.

Figures S4 and S5 display measurements of strong photothermal effects in the silicon cantilever. In the case of Fig. S4, this was performed with a constant drive frequency $f \approx 124.28\,\text{kHz}$, which is on the edge of flat-top response. Although the laser power used was identical to those in Figs. S1–S3, a lock-in frequency sweep immediately preceding Fig. S4 measurements showed a flat-top response in the range $f \approx 124.2\,\text{kHz}$ to $f \approx 124.28\,\text{kHz}$. The shift in this flat-top frequency range was likely due to a change in laser focal plane between Fig. S4 and Figs. S1–S3, which would impact the total absorbed laser power. Figure S4(c) shows that R values are roughly constant all along the cantilever length. The equilibrium profile z_0 is nearly identical to those in Fig. S2(c).

Figure S5 shows oscilloscope measurements of the cantilever response during upward and downward sweeps of the drive frequency. The laser was focused near the cantilever free end. The flat-top response is observed only during the downward sweep, and saturated with an amplitude of $R \approx 2.6\,\lambda$.

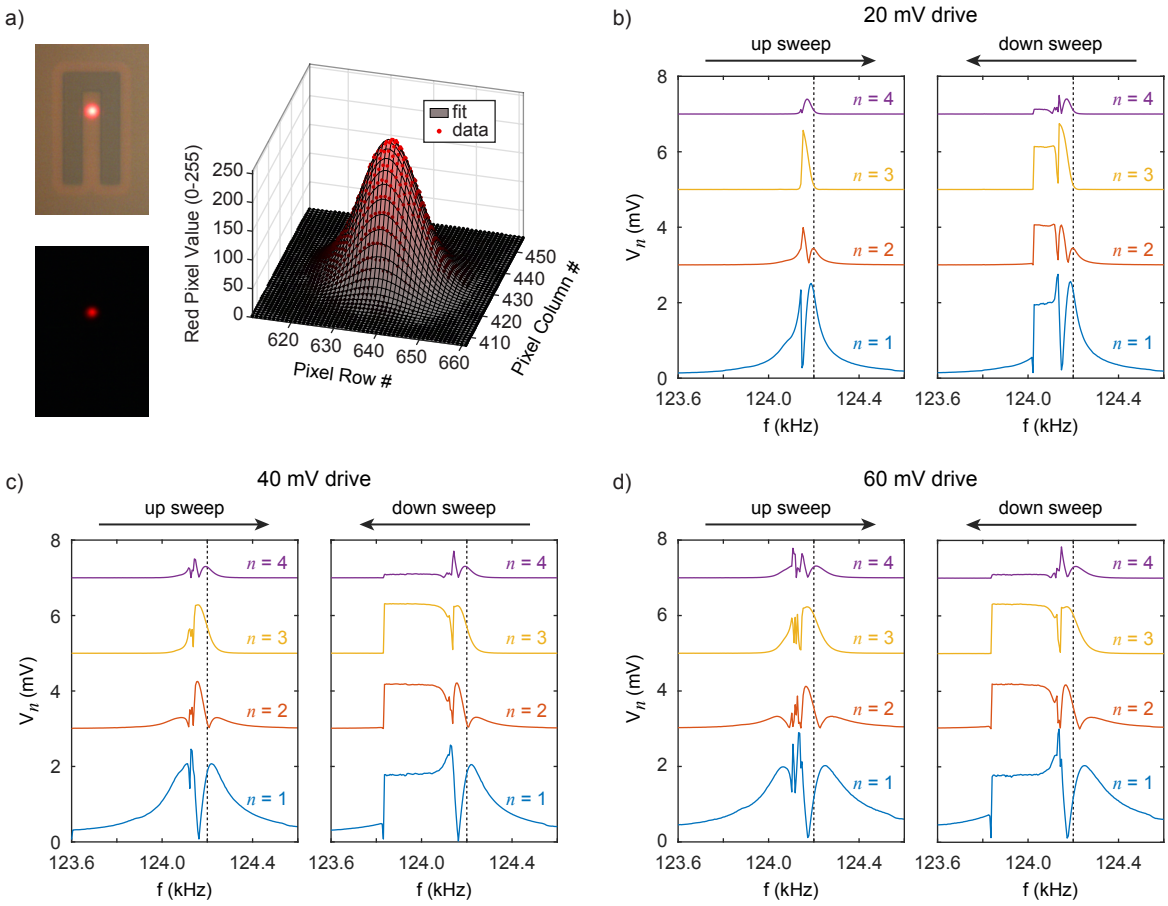

FIG. S1. (a) The silicon cantilever under test and a measurement of the laser spot diameter. Left panels: Images of the silicon cantilever and laser as viewed by the camera in our setup. Images are shown with white light illumination turned on (top) and turned off (bottom). Right panel: A surface plot showing 8-bit values of the red pixels in the left-bottom image. A Gaussian fit gives a $1/e^2$ diameter of ≈ 26 pixels, which corresponds to $\approx 7\,\mu$m. (b)–(d) Lock-in measurements of the silicon cantilever showing hysteresis and optomechanical self-oscillation. All measurements were made with the laser focused near the cantilever tip and $\approx 20\,\mu$W laser power. In all plots, upward and downward frequency sweeps are measured by the lock-in at integer harmonics of the drive frequency, f. Only the amplitudes, V_n, of these harmonics are shown, although phases were also collected. All downward sweeps contain a narrow frequency range in which all four harmonics have a flat amplitude response. This is the region of optomechanical self-oscillation with entrainment to the inertial drive. Vertical dashed lines show the frequency at which data in Figs. S2 and S3 was taken. Excitation voltages are (b) 20 mV, (c) 40 mV, and (d) 60 mV.

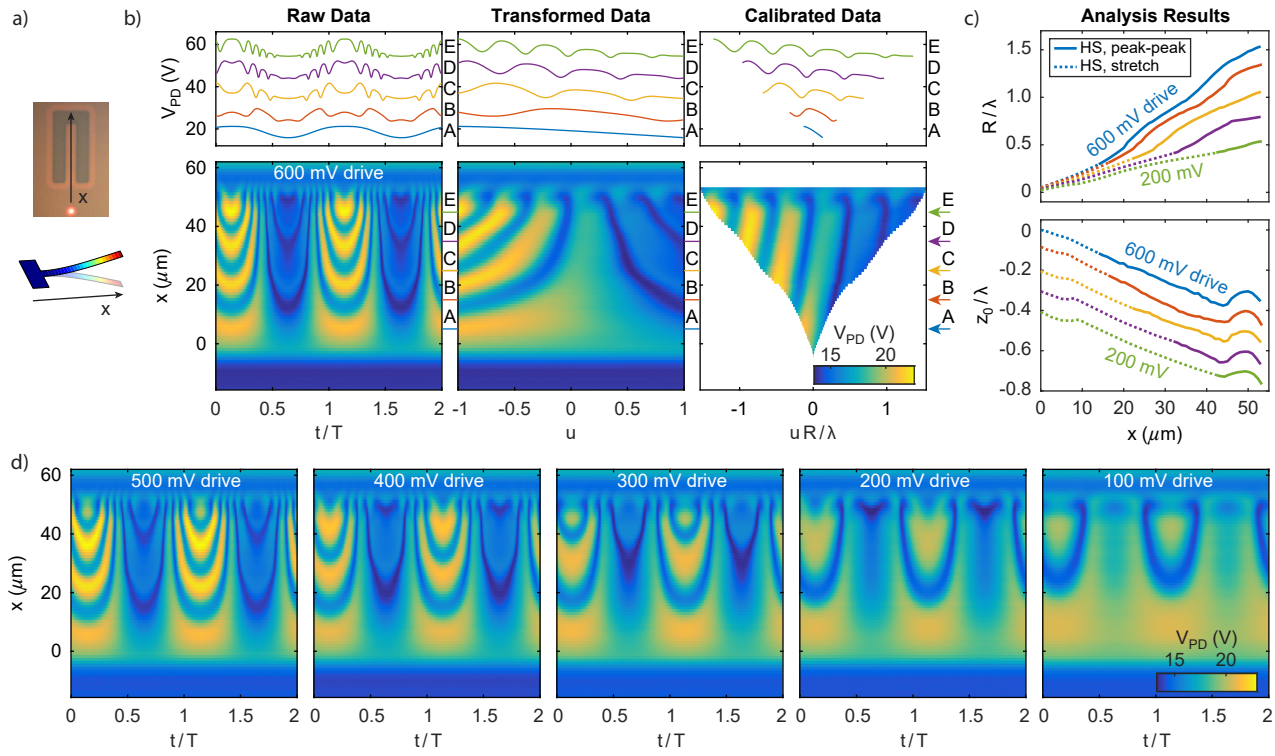

FIG. S2. Measurements taken while scanning the detection laser along the length of a silicon cantilever. These results were recorded using $\approx 20\,\mu$W laser power. (a) Laser starting position as viewed by the camera in our setup (top) and a schematic of the cantilever vibrational mode and laser scan direction (bottom). (b)–(d) Data taken while exciting the cantilever fundamental mode with $f \approx 124.2\,$kHz and scanning the laser position x in $\approx 1\,\mu$m steps. The cantilever base and free end are at located at $x \approx 0\,\mu$m and $x \approx 50\,\mu$m, respectively. (b) Data taken with a drive voltage of $\approx 600\,$mV applied to the piezoelectric disk. Left panels: Raw oscilloscope data plotted versus normalized time, t/T, where $T = f^{-1}$. Middle panels: The same data after the $t \to u$ transformation. Right panels: The same data after distance calibration. Upper panels display individual oscilloscope traces taken from the lower panels at the x coordinates indicated by arrows labeled A through E. The data in the upper panels are shifted vertically for clarity. The data in the lower panels use the same color scale. (c) Vibration amplitudes R and equilibrium positions z_0 determined by applying the horizontal slice (HS) peak-to-peak and stretch methods to the data in (b) and (d). (d) Raw oscilloscope data for drive voltages of $\approx 500\,$mV to $\approx 100\,$mV. All panels use the same color scale.

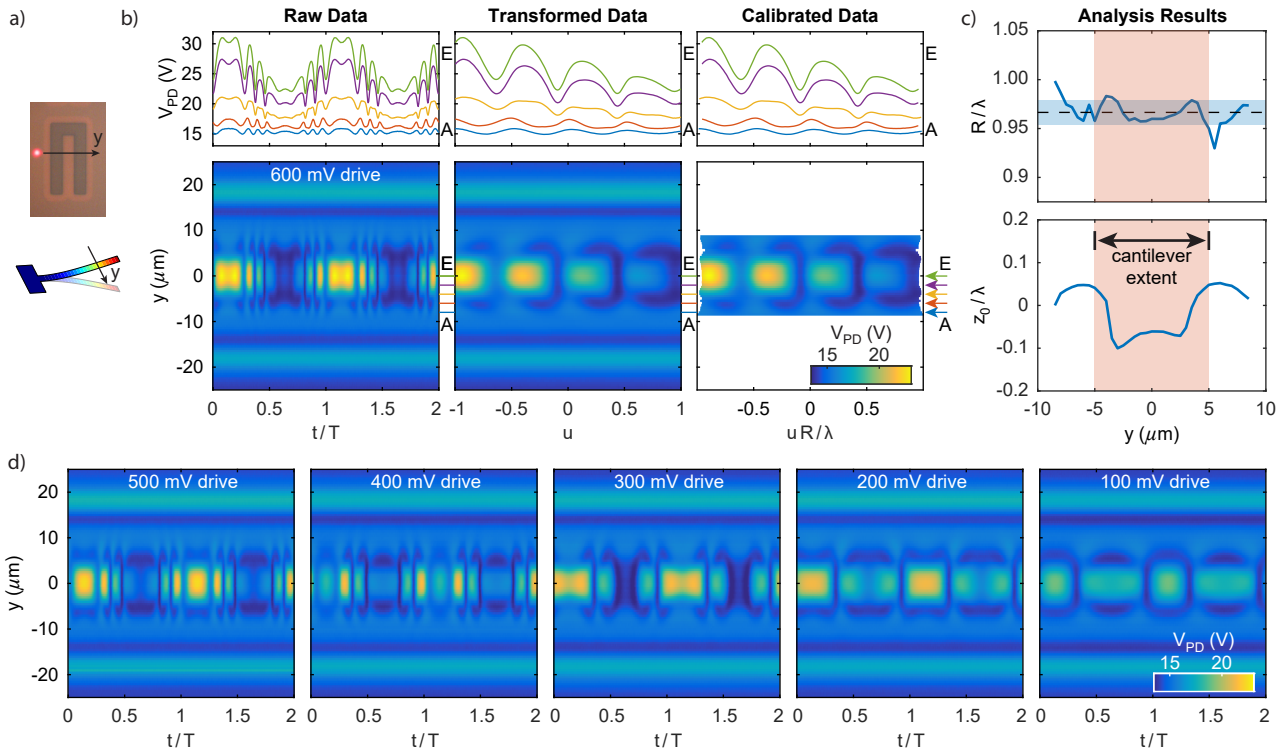

FIG. S3. Measurements taken while scanning the detection laser across the width of a silicon cantilever. These results were recorded using $\approx 20\,\mu$W laser power. (a) Laser starting position as viewed by the camera in our setup (top) and a schematic of the cantilever vibrational mode and laser scan direction (bottom). (b)–(d) Data taken while exciting the cantilever fundamental mode with $f \approx 124.2\,$kHz and scanning the laser position y in $\approx 0.5\,\mu$m steps. The cantilever edges are located at $y \approx \pm 5\,\mu$m. (b) Data taken with a drive voltage of $\approx 600\,$mV. The data is presented in a similar format to Fig. S2(b). (c) R and z_0 values determined by applying the HS peak-to-peak method to the data in (b). Consistent R values are measured even when the laser center is off of the cantilever. Using all of the R values shown, the arithmetic mean (dashed line) and standard deviation (shaded horizontal band) are $R = (0.97 \pm 0.01)\lambda$. (d) Raw oscilloscope data for drive voltages of $\approx 500\,$mV to $\approx 100\,$mV. All panels use the same color scale.

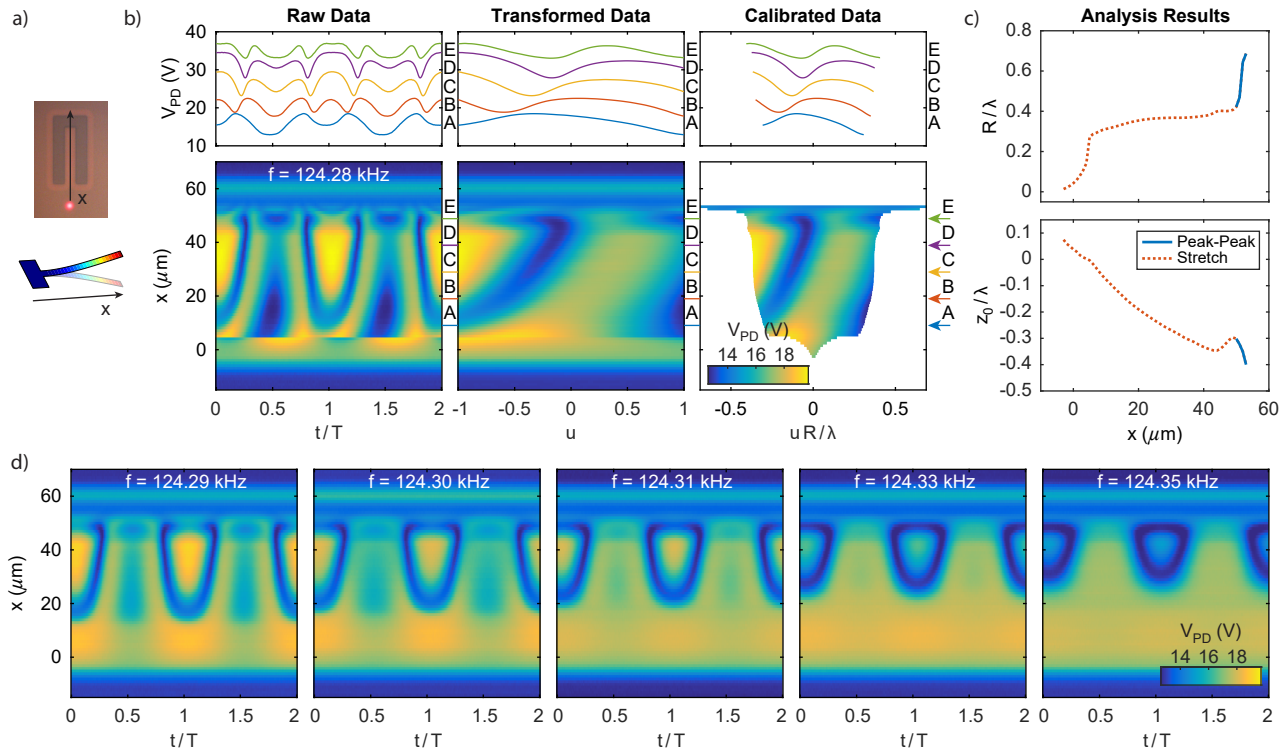

FIG. S4. Entrained self-oscillation of a silicon cantilever measured while scanning the laser along the cantilever length. These results were recorded using a laser power of $\approx 20\,\mu$W and a drive frequency near the threshold for self-oscillation. (a) Laser starting position as viewed by the camera in our setup (top), and schematic of the cantilever vibrational mode and laser scan direction (bottom). (b)–(d) Data taken while driving the cantilever with a voltage of $\approx 20\,$mV and scanning the laser position x in $\approx 1\,\mu$m steps. The cantilever base and free end are at located at $x \approx 0\,\mu$m and $x \approx 50\,\mu$m, respectively. (b) Data taken with an drive frequency of $\approx 124.28\,$kHz. Immediately preceding this scan, a lock-in sweep was performed to locate the onset of self-oscillation. Self-oscillation occurred for frequencies below $f \approx 124.28\,$kHz. The data is presented in a similar format to Fig. S2(b). (c) R and z_0 values determined by applying the HS peak-to-peak and stretch methods to the data in (b). The trend in R values is nearly flat all along the cantilever length, which suggests that vibration amplitudes are amplified and self-limited by the laser wavelength. (d) Raw oscilloscope data for drive frequencies gradually moving away from the cantilever resonance. All panels use the same color scale.

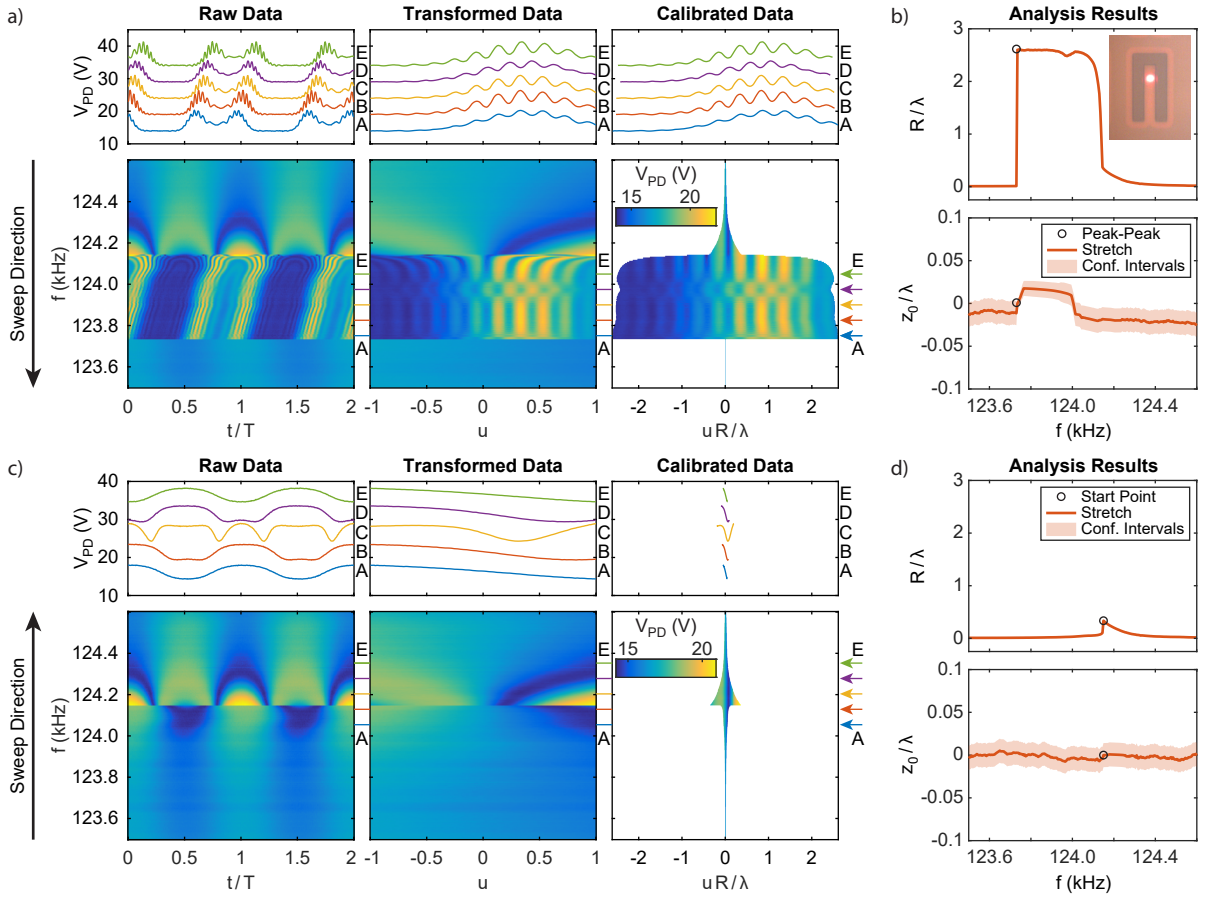

FIG. S5. Oscilloscope measurements of entrained self-oscillation in the silicon cantilever. These results were recorded using a drive voltage of $\approx 40\,\mathrm{mV}$ and laser power of $\approx 20\,\mu\mathrm{W}$. (a) Measurements during a downward sweep of the drive frequency presented in a similar format to Fig. S2(b). (b) R and z_0 values extracted from (a). Confidence intervals for R are smaller than the line width. R shows a wide region of entrainment in which amplitudes are a constant $\approx 2.5\lambda$. For z_0 values, confidence intervals (one standard deviation) resulting from the stretch method fits are shown. Inset: Image of the laser position as viewed by the camera in our setup. (c) and (d) Similar results to (a) and (b), but for an upward sweep of the drive frequency. In (d), the stretch method fitting is initiated at the frequency marked by an open circle using a calibrated interference pattern $V_{\mathrm{PD}}(z)$ from the down sweep data as reference.

B. Measurements of a $\approx 2.5\,\mu$m wide cantilever

Measurements of a $\approx 2.5\,\mu$m-wide silicon cantilever are shown in Fig. S6. As these results show, R and z_0 values can be reliably measured despite the fact that the cantilever width is smaller than our $w \approx 7\,\mu$m laser spot. Both lock-in and oscilloscope measurements are slightly noisier than similar measurements of the $\approx 10\,\mu$m-wide cantilever. Despite this, a flat-top region is clearly discernable in Fig. S6(b), and uncertainties in R and z_0 in Fig. S6(d) are smaller than the line width. Perhaps the most noticeable consequence of the narrow beam width is its impact on the observed interference patterns, as shown in the upper panels of Fig. S6(c). The calibrated versions of oscilloscope traces B and C show distortions to some of the interference peaks and valleys that was not observed in any of the $\approx 10\,\mu$m-wide cantilever measurements. Because of these distortions, we opted to use the horizontal slice (HS) stretch method to determine R and z_0 for most of the x coordinates in Fig. S6(d). This reduced the risk of false peaks and valleys detected using the peak-to-peak method.

These results suggest that our calibration technique can be applied to MEMS/NEMS cantilevers narrower than those we have tested. It is our suspicion that even cantilevers narrower than λ are amenable to our technique. We suspect that the primary complications that will arise as cantilever dimensions continue to shrink will be worsening signal-to-noise ratios and increased diffraction effects leading to larger distortions of the observed interference patterns. Despite these distortions, the stretch method will still enable direct comparison between oscilloscope measurements, meaning that linear changes in R and z_0 will remain discernable.

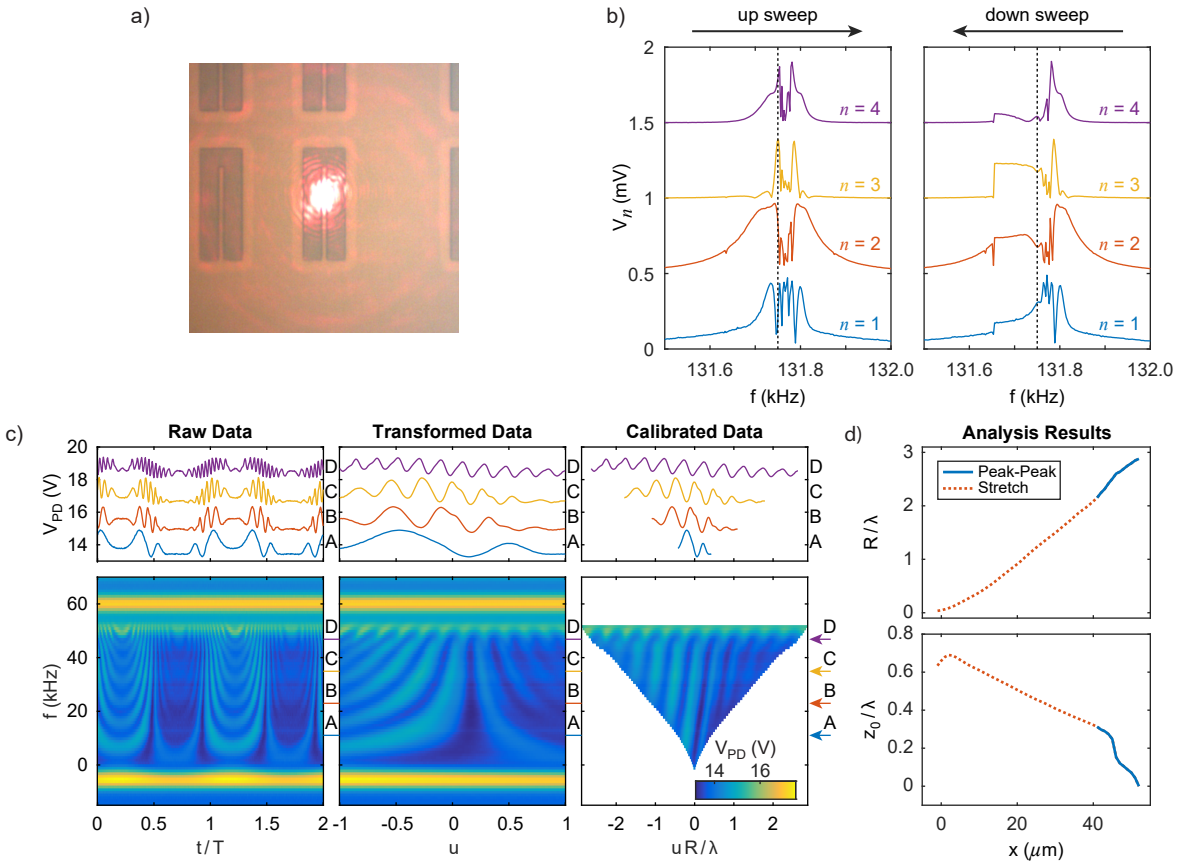

FIG. S6. Measurements taken while scanning the laser along the length of a narrow silicon cantilever. These results were recorded using $\approx 20\,\mu$W laser power and $\approx 40\,$mV drive voltage. (a) The cantilever and laser spot as viewed by the camera in our setup (top). (b) Lock-in measurements of the cantilever during sweeps of the drive frequency as measured near the cantilever free end. In the downward sweep, a region of entrained self-oscillation can be seen between $f \approx 131.65\,$kHz and $f \approx 131.75\,$kHz. Vertical dashed lines denote the drive frequency used in (c). The drive frequency in (c) was approached using an up sweep. (c) Data taken while exciting the cantilever fundamental mode with $f \approx 131.75\,$kHz and scanning the laser position x in $\approx 1\,\mu$m steps. The cantilever base and free end are at located at $x \approx 0\,\mu$m and $x \approx 50\,\mu$m, respectively. The data is presented in a similar format to Fig. S2(b). (d) R and z_0 values determined by applying the HS peak-to-peak and stretch methods to the data in (c). Uncertainties in R and z_0 are smaller than the line width.

S2. IMPACT OF SUBSTRATE ROUGHNESS ON THE INTERFEROMETRIC SIGNAL STRENGTH

All devices studied in this work utilize silicon substrates. In each case, the sacrificial oxide was removed by a highly selective hydrofluoric acid etch, leaving the underlying substrate optically smooth. In designing MEMS/NEMS devices to be measured by Fabry-Perot interferometry, surface roughness must be considered. For example, increased surface roughness randomly diffuses the reflected laser light, degrading the quality and the intensity of the light directed back towards the photodetector.

To determine the effect of surface roughness on the interferometric signal strength, an analytic expression first proposed by Mahajan [10] can be used to compute the Strehl ratio of an optical image with random wavefront aberrations. In the present context of laser interferometry, the Strehl ratio, S, is defined as the ratio of the on-axis intensity of a laser beam reflected by a substrate with surface aberrations to the on-axis intensity of a laser beam reflected by an ideally smooth substrate. For a substrate with a root-mean-square surface roughness given by σ, Mahajan's formula gives $S \approx \exp\left(-(2\pi\sigma/\lambda)^2\right)$.

Because our readout system combines light reflected from the MEMS/NEMS device (with on-axis intensity I_1) with light reflected by the substrate (with on-axis intensity I_2), the on-axis intensity of the interference signal measured by our photodetector is proportional to $\sqrt{I_1 I_2}$. Therefore, Mahajan's formula suggests that compared to an ideally smooth substrate, our interferometric signal decreases by half (i.e. $S \approx 0.25$) when the substrate roughness is $\sigma/\lambda \approx 0.19$. For red light ($\lambda \approx 640\,\text{nm}$), this corresponds to $\sigma \approx 120\,\text{nm}$.

S3. IMPACT OF INERTIAL DRIVE ON THE NONLINEAR EQUATION OF MOTION

Because our experiment is performed using inertial drive rather than an external drive force (e.g. electrostatic or magnetic drive), we must clarify how this inertial force enters the equation of motion. A MEMS/NEMS resonator with an external drive can be modeled by the single-degree-of-freedom system pictured in Fig. S7(a). Here, the mass m oscillates along the x axis under the influence of a drive force $F_D = F\cos(\omega t)$. This drive force has amplitude F and angular frequency ω. In relation to the drive frequency f used in our experiments, the angular drive frequency is $\omega = 2\pi f$. The mass is attached to an anchor by a spring and damper, which account for the elasticity and internal friction of the MEMS/NEMS resonator. The spring constant is given by $k = m(\omega_0^2 + \alpha_2 x + \alpha_3 x^2)$, where ω_0 is the angular resonant frequency and α_2, α_3 are the nonlinear stiffening coefficients from Eq. 3 of the main text. The damping constant is $c = m\gamma$, where $\gamma = \omega_0/Q$ and Q is the resonator's quality factor. In response to motion along the x axis, the resonator experiences a spring force $F_s = -kx$ and damping force $F_c = -c\dot{x}$ that counteract its motion. Here, $\dot{x} = dx/dt$ is the resonator velocity. Under the influence of drive, spring, and damping forces, Newton's second law reveals that the resonator obeys the following equation of motion:

$$\ddot{x} + \gamma\dot{x} + \omega_0^2 x + \alpha_2 x^2 + \alpha_3 x^3 = \frac{F}{m}\cos\omega t, \tag{S1}$$

where $\ddot{x} = d^2x/dt^2$ is the resonator acceleration.

The case of inertial driving is shown in Fig. S7(b). Here, the entire system is shaken so that the spring's base has position $x_b = X_b\cos\omega t$. The shaking is described by amplitude X_b and angular frequency ω. In this case, the spring extension is no longer equal to x, but to $(x - x_b)$. Therefore, the nonlinear spring constant is $k = m(\omega_0^2 + \alpha_2(x - x_b) + \alpha_3(x - x_b)^2)$. The spring and damping forces become $F_s = -k \cdot (x - x_b)$ and $F_c = -c \cdot (\dot{x} - \dot{x}_b)$, respectively. Newton's second law then gives

$$\ddot{x} + \gamma(\dot{x} - \dot{x}_b) + \omega_0^2(x - x_b) + \alpha_2(x - x_b)^2 + \alpha_3(x - x_b)^3 = 0. \tag{S2}$$

If we add $-\ddot{x}_b$ to both sides of this equation and define a new variable $y = x - x_b$, this becomes

$$\ddot{y} + \gamma\dot{y} + \omega_0^2 y + \alpha_2 y^2 + \alpha_3 y^3 = -\omega^2 X_b\cos\omega t. \tag{S3}$$

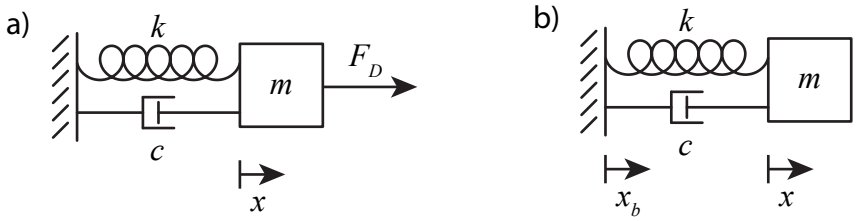

FIG. S7. Single-degree-of-freedom resonators with (a) external driving, and (b) inertial driving.

The above equation exactly resembles Eq. S1, except with the substitutions $x \to y$ and $F/m \to -\omega^2 X_b$. Therefore, the inertially driven system behaves identically to the externally driven system when viewed in terms of relative motion, y, between the mass and base. This is fortuitous for MEMS/NEMS interferometry since our experimental setup directly detects the relative motion between the resonator and bulk substrate, which is rigidly anchored to the resonator base.

S4. PERTURBATION THEORY, CUBIC NONLINEARITY

The equation of a damped, harmonically driven Duffing oscillator is

$$\ddot{x} + \gamma\dot{x} + \omega_0^2 x + \alpha x^3 = \kappa \cos \omega t, \tag{S4}$$

where κ is a generic driving term. As described in Section S3, this equation is valid both for external driving and inertial driving. In the case of external driving, x is motion in an inertial reference frame, and $\kappa = F/m$. In the case of inertial driving, x is motion relative to the resonator's base, and $\kappa = -\omega^2 X_b$. Following the work of other authors [11, 12], we will solve this equation perturbatively by scaling γ, α, and κ by a small dimensionless parameter ϵ and then solve for x as a power series in ϵ. At the end of our calculations, we will set $\epsilon = 1$. The essence of this approach is therefore to treat the damping, nonlinear force, and excitation force as perturbations to a simple harmonic oscillator.

For convenience in the derivation that follows, we will rearrange Eq. S4 as

$$\ddot{x} + \omega^2 x = \left(\omega^2 - \omega_0^2\right) x - \gamma\dot{x} - \alpha x^3 + \kappa \cos \omega t, \tag{S5}$$

where a factor of $\omega^2 x$ has been added to both sides of the equation. We will now treat everything on the right hand side as a perturbation:

$$\ddot{x} + \omega^2 x = \epsilon \left[\left(\omega^2 - \omega_0^2\right) x - \gamma\dot{x} - \alpha x^3 + \kappa \cos \omega t\right]. \tag{S6}$$

Our solution for x will take the form:

$$x = x_0 + \epsilon^1 x_1 + \epsilon^2 x_2 + \ldots. \tag{S7}$$

By treating the term $(\omega^2 - \omega_0^2)$ in Eq. S6 as a small perturbation, we are implicity assuming that the drive frequency ω is near the resonance ω_0. If we define a detuning parameter as $\sigma = \omega - \omega_0$, this assumption becomes $|\sigma/\omega_0| \ll 1/2$. This is a slightly stricter restriction than the derivations of Refs. 11, 12, which assume $|\sigma/\omega_0| \ll 1$. However, our approach will benefit greatly from this assumption. Compared to the derivations in Refs. 11, 12, which stop at order ϵ^1 and use the method of multiple scales, our approach gives the steady state behavior of x at higher orders of ϵ with far less algebra. This is because our derivation assumes from the start that x is periodic with period ω^{-1}, and is not concerned with any time scales other than ωt, such as a "slow time" ϵt that describes the approach to periodic

behavior. Because we exclude other time scales, our approach cannot be used to determine whether a solution for x is stable or unstable. However, during our derivation, we will refer to Refs. 11, 12 to determine which solutions are stable.

A. Solution at order ϵ^0

Writing out Eq. S6 to order ϵ^0 gives:

$$\ddot{x}_0 + \omega^2 x_0 = 0, \tag{S8}$$

whose solution is

$$x_0 = \frac{1}{2} A_0 e^{i\omega t} + \text{c.c.}, \tag{S9}$$

where "c.c." represents the complex conjugate of the preceding terms. A_0 is the complex amplitude of the response. To determine the value of A_0, we must proceed to the next order in perturbation theory.

B. Solution at order ϵ^1

We first note that x_0^3 can be written as:

$$x_0^3 = \frac{1}{8}\left(A_0^3 e^{i3\omega t} + 3|A_0|^2 A_0 e^{i\omega t}\right) + \text{c.c.}, \tag{S10}$$

where, again, "c.c." represents the complex conjugate of the preceeding terms. Writing out Eq. S6 to order ϵ^1 then gives:

$$\ddot{x}_1 + \omega^2 x_1 = \frac{1}{2}\left\{\left[\omega^2 - \omega_0^2 - i\omega\gamma - \frac{3}{4}\alpha|A_0|^2\right] A_0 + \kappa\right\} e^{i\omega t} - \frac{1}{8}\alpha A_0^3 e^{i3\omega t} + \text{c.c.}. \tag{S11}$$

In order for x_1 not to grow infinitely large, the terms in curly brackets – known as "secular terms" – must vanish. Thus we have

$$\left[\omega^2 - \omega_0^2 - i\omega\gamma - \frac{3}{4}\alpha|A_0|^2\right] A_0 + \kappa = 0, \tag{S12}$$

which, after rearranging, leads to

$$A_0 = \frac{-\kappa}{\omega^2 - \omega_0^2 - \frac{3}{4}\alpha|A_0|^2 - i\omega\gamma}. \tag{S13}$$

On its surface, this result differs slightly from the order ϵ^1 solution in Ref. 11. However, to within the accuracy provided by our original assumption of small detuning $\sigma = (\omega - \omega_0) \ll \omega_0$, the above result is equivalent to

$$A_0 = \frac{-\kappa/(2\omega_0)}{\omega - \omega_0 - (3\alpha|A_0|^2)/(8\omega_0) - i\gamma/2}. \tag{S14}$$

The equivalence of these two equations can be proven by substituting σ into Eq. S13 and carefully applying the approximation $\sigma/\omega_0 \approx 0$. Equation S14 matches the results of Refs. 11, 12 in both amplitude and phase. This shows that as a function of ω, the lowest-order response of the Duffing oscillator is functionally identical to the Lorentzian response of a linear harmonic oscillator, but with one added term that couples the amplitude $|A_0|$ to the resonant frequency. We can therefore define a nonlinear resonant frequency, ω_{NL}, as

$$\omega_{\mathrm{NL}} = \omega_0 + \frac{3\alpha|A_0|^2}{8\omega_0}. \tag{S15}$$

Equations S13 and S14 are implicit equations for A_0. To solve for A_0, one must first take the absolute value (squared) of either of these equations, and then rearrange it as a polynomial in $|A_0|^2$. In doing so, one will find that this is a third-order polynomial, and therefore there are three complex solutions for $|A_0|^2$. For any set of parameters $(\omega, \omega_0, \kappa, \gamma, \alpha)$, one will find that either three real and positive solutions for $|A_0|^2$ exist, or only one such solution exists. This is consistent with the plot of $|A_0|$ versus ω in Fig. 3b of the main text, where we see that this function resembles a Lorentzian curve that has been tilted to one side. At any frequency ω, the function is either single-valued or triple-valued. In terms of stability, Refs. 11, 12 prove that when the solution is single-valued it is stable, and when it is triple-valued the only unstable solution is the median value.

The non-secular terms in Eq. S11 lead to

$$\ddot{x}_1 + \omega^2 x_1 = -\frac{1}{8}\alpha A_0^3 e^{i3\omega t} + \text{c.c.}. \tag{S16}$$

The general solution to this equation (homogenous solution plus particular solution) is

$$x_1 = \frac{1}{2}A_1 e^{i\omega t} + \frac{1}{2}B_1 e^{i3\omega t} + \text{c.c.}, \tag{S17}$$

where A_1 can only be found by going to the next level of perturbation theory. Solving for B_1 gives

$$B_1 = \frac{\alpha A_0^3}{32\omega^2}. \tag{S18}$$

C. Solution at order ϵ^2

Before writing Eq. S6 to order ϵ^2, we first note that x^3 can be approximated (to order ϵ^1) by

$$\begin{aligned} x^3 &= (x_0 + \epsilon x_1)^3 \\ &\approx x_0^3 + 3\epsilon x_0^2 x_1. \end{aligned} \tag{S19}$$

Plugging the functional forms of x_0 and x_1 into $x_0^2 x_1$ gives

$$\begin{aligned} x_0^2 x_1 =& \frac{1}{8}\left(2|A_0|^2 A_1 + A_0^2 A_1^* + A_0^{*2} B_1\right) e^{i\omega t} \\ &+ \frac{1}{8}\left(2|A_0|^2 B_1 + A_0^2 A_1\right) e^{i3\omega t} + \frac{1}{8} A_0^2 B_1 e^{i5\omega t} + \text{c.c.}. \end{aligned} \tag{S20}$$

Here A_n^* denotes the complex conjugate of A_n. Writing Eq. S6 to order ϵ^2 thus gives:

$$\begin{aligned} \ddot{x}_2 + \omega^2 x_2 &= \left(\omega^2 - \omega_0^2\right) x_1 - \gamma \dot{x}_1 - 3\alpha x_0^2 x_1 \\ &= \frac{1}{2}\left[\left(\omega^2 - \omega_0^2 - i\omega\gamma\right) A_1 - \frac{3\alpha}{4}\left(2|A_0|^2 A_1 + A_0^2 A_1^* + A_0^{*2} B_1\right)\right] e^{i\omega t} \\ &+ \frac{1}{2}\left[\left(\omega^2 - \omega_0^2 - i3\omega\gamma\right) B_1 - \frac{3\alpha}{4}\left(2|A_0|^2 B_1 + A_0^2 A_1\right)\right] e^{i3\omega t} \\ &- \frac{3\alpha}{8} A_0^2 B_1 e^{i5\omega t} + \text{c.c.}. \end{aligned} \tag{S21}$$

Removing secular terms leads to:

$$\left(\omega^2 - \omega_0^2 - \frac{3\alpha}{2}|A_0|^2 - i\omega\gamma\right) A_1 = \frac{3\alpha}{4}\left(A_0^2 A_1^* + A_0^{*2} B_1\right), \tag{S22}$$

which can be solved for A_1 (e.g. by complex conjugating the entire equation, then combining both equations to eliminate A_1^*). The solution is

$$A_1 = \frac{3\alpha^2 |A_0|^4 A_0}{128\omega^2} \frac{\omega^2 - \omega_0^2 - \frac{3}{4}\alpha|A_0|^2 + i\omega\gamma}{\left(\omega^2 - \omega_0^2 - \frac{3}{2}\alpha|A_0|^2\right)^2 + (\omega\gamma)^2 - \left(\frac{3}{4}\alpha|A_0|^2\right)^2}. \tag{S23}$$

The full solution of Eq. S21 is then:

$$x_2 = \frac{1}{2} A_2 e^{i\omega t} + \frac{1}{2} B_2 e^{i3\omega t} + \frac{1}{2} C_2 e^{i5\omega t} + \text{c.c.}, \tag{S24}$$

where

$$B_2 = -\frac{1}{8\omega^2}\left[\left(\omega^2 - \omega_0^2 - i3\omega\gamma\right) B_1 - \frac{3\alpha}{4}\left(2|A_0|^2 B_1 + A_0^2 A_1\right)\right], \tag{S25}$$

$$\begin{aligned} C_2 &= \frac{\alpha}{32\omega^2} A_0^2 B_1 \\ &= \left(\frac{\alpha}{32\omega^2}\right)^2 A_0^5, \end{aligned} \tag{S26}$$

and A_2 can only be found by going to the next level of perturbation theory.

D. Solution at order ϵ^3

Here we're only interested in removing secular terms, since they will give us an expression for A_2. We note that x^3 is given (to second order in ϵ) by:

$$\begin{aligned} x^3 &= (x_0 + \epsilon x_1 + \epsilon^2 x_2)^3 \\ &= x_0^3 + 3\epsilon x_0^2 x_1 + 3\epsilon^2 x_0 x_1^2 + 3\epsilon^2 x_0^2 x_2. \end{aligned} \tag{S27}$$

The first of these terms in ϵ^2 can be expressed as

$$\begin{aligned} x_0 x_1^2 =& \frac{1}{8}\left(A_0^* A_1^2 + 2A_0^* A_1^* B_1 + 2A_0|A_1|^2 + 2A_0|B_1|^2\right) e^{i\omega t} \\ &+ \frac{1}{8}\left(2A_0^* A_1 B_1 + A_0 A_1^2 + 2A_0 A_1^* B_1\right) e^{i3\omega t} \\ &+ \frac{1}{8}\left(A_0^* B_1^2 + 2A_0 A_1 B_1\right) e^{i5\omega t} + \frac{1}{8} A_0 B_1^2 e^{i7\omega t} + \text{c.c.}, \end{aligned} \tag{S28}$$

and similarly for the second term in ϵ^2

$$\begin{aligned} x_0^2 x_2 =& \frac{1}{8}\left(2|A_0|^2 A_2 + A_0^{*2} B_2 + A_0^2 A_2^*\right) e^{i\omega t} + \frac{1}{8}\left(2|A_0|^2 B_2 + A_0^{*2} C_2 + A_0^2 A_2\right) e^{i3\omega t} \\ &+ \frac{1}{8}\left(2|A_0|^2 C_2 + A_0^2 B_2\right) e^{i5\omega t} + \frac{1}{8} A_0^2 C_2 e^{i7\omega t} + \text{c.c.}. \end{aligned} \tag{S29}$$

Writing Eq. S6 to order ϵ^3 then gives:

$$\ddot{x}_3 + \omega^2 x_3 = \left(\omega^2 - \omega_0^2\right) x_2 - \gamma \dot{x}_2 - 3\alpha\left(x_0 x_1^2 + x_0^2 x_2\right). \tag{S30}$$

The secular terms in this equation would then give

$$\begin{aligned} &\left(\omega^2 - \omega_0^2 - i\omega\gamma - \frac{3\alpha}{2}|A_0|^2\right) A_2 = \\ &\qquad \frac{3\alpha}{4}\left(A_0^* A_1^2 + 2A_0^* A_1^* B_1 + 2A_0|A_1|^2 + 2A_0|B_1|^2 + A_0^{*2} B_2 + A_0^2 A_2^*\right), \end{aligned} \tag{S31}$$

which can be solved numerically for A_2.

If we wish to see the effect of the $e^{i7\omega t}$ term on x_3, we can start with the ansatz $x_3 = \frac{1}{2} D_3 e^{i7\omega t} + \frac{1}{2} C_3 e^{i5\omega t} + \frac{1}{2} B_3 e^{i3\omega t} + \frac{1}{2} A_3 e^{i\omega t} + \text{c.c.}$ to find

$$\begin{aligned} D_3 &= \frac{\alpha}{64\omega^2}(A_0^2 C_2 + A_0 B_1^2) \\ &= \left(\frac{\alpha}{32\omega^2}\right)^3 A_0^7. \end{aligned} \tag{S32}$$

E. Summary

In summary, the solution to the driven, damped Duffing equation is:

$$x = \frac{1}{2}Ae^{i\omega t} + \frac{1}{2}Be^{i3\omega t} + \frac{1}{2}Ce^{i5\omega t} + \frac{1}{2}De^{i7\omega t} + \cdots + \text{c.c.}, \tag{S33}$$

with

$$A = A_0 + A_1 + A_2 + \ldots \tag{S34}$$

$$B = B_1 + B_2 + \ldots \tag{S35}$$

$$C = C_2 + \ldots \tag{S36}$$

$$D = D_3 + \ldots \tag{S37}$$

Going to higher levels of perturbation theory will continue to add higher (odd integer) frequency components to x. Furthermore, each new level will add slight corrections to the existing frequency components.

It is instructive to examine at the leading terms in A, B, C, etc. If we wish to compare the magnitudes of the higher harmonics (B, C, etc.) to A, we can get a good estimate by looking at the leading terms. What we find is:

$$\frac{|B_1|}{|A_0|} = \left|\frac{\alpha A_0^3}{32\omega^2}\right| \frac{1}{|A_0|} = \frac{|\alpha|}{32\omega^2}\frac{|A_0|^3}{|A_0|} = \frac{|\alpha|\,|A_0|^2}{32\omega^2}, \tag{S38}$$

$$\frac{|C_2|}{|A_0|} = \left|\frac{\alpha}{32\omega^2}\right|^2 \frac{|A_0|^5}{|A_0|} = \left(\frac{|B_1|}{|A_0|}\right)^2, \tag{S39}$$

$$\frac{|D_3|}{|A_0|} = \left|\frac{\alpha}{32\omega^2}\right|^3 \frac{|A_0|^7}{|A_0|} = \left(\frac{|B_1|}{|A_0|}\right)^3. \tag{S40}$$

As we showed in Sec. S4 B, a Duffing nonlinearity shifts the resonant frequency of an oscillator to $\omega_{\text{NL}} = \omega_0 + (3\alpha|A_0|^2)/(8\omega_0)$. The fractional shift in resonant frequency caused by the Duffing nonlinearity is thus

$$\frac{\Delta\omega}{\omega_0} = \frac{\omega_{\text{NL}} - \omega_0}{\omega_0} = \frac{3\alpha|A_0|^2}{8\omega_0^2}. \tag{S41}$$

Therefore, the above expression for $|B_1|/|A_0|$ becomes simply

$$\frac{|B_1|}{|A_0|} = \frac{1}{12}\left|\frac{\Delta\omega}{\omega_0}\right|\frac{\omega_0^2}{\omega^2} \approx \frac{1}{12}\left|\frac{\Delta\omega}{\omega_0}\right|, \tag{S42}$$

where, again, the approximate sign above must be valid because we have assumed from the outset that ω is near ω_0, and therefore $\omega_0/\omega \approx 1$. While we have not strictly proven that

the solutions we have obtained for B_1, C_2, and D_3 are stable, we infer that they must be stable. This is based on the fact that unlike A_0, which can be multi-valued as discussed in Sec. S4 B, our solutions for B_1, C_2, and D_3 are strictly single-valued. In the case of A_0, initial conditions near the unstable solution will equilibrate to one of the stable solutions over time. This is not possible with B_1, C_2, and D_3. If any one of these is unstable, then x itself is unstable, violating our original assumption of periodic motion.

S5. PERTURBATION THEORY, QUADRATIC AND CUBIC NONLINEARITIES

In some circumstances, a MEMS/NEMS system can have a quadratic as well as cubic nonlinearity. In fact, a change in the equilibrium position of an oscillator during driving (as we have observed experimentally) can only be explained by an even-order nonlinearity. We will consider the following equation of motion

$$\ddot{x} + \gamma\dot{x} + \omega_0^2 x + \alpha_2 x^2 + \alpha_3 x^3 = \kappa \cos\omega t, \tag{S43}$$

which is identical to Eq. S4, with the addition of the $\alpha_2 x^2$ term. As in the previous derivation, we will rewrite this equation as

$$\ddot{x} + \omega^2 x = (\omega^2 - \omega_0^2)x - \gamma\dot{x} - \alpha_2 x^2 - \alpha_3 x^3 + \kappa \cos\omega t. \tag{S44}$$

Following the lead of Ref. 11, this equation is easiest to solve perturbatively if the α_2 term is scaled by ϵ and all other terms terms are scaled by ϵ^2. Thus the equation to solve becomes:

$$\ddot{x} + \omega^2 x = -\epsilon\alpha_2 x^2 + \epsilon^2 \left[\left(\omega^2 - \omega_0^2\right) x - \gamma\dot{x} - \alpha_3 x^3 + \kappa \cos\omega t\right]. \tag{S45}$$

We will now solve this equation to order ϵ^2 with a solution of the form $x = x_0 + \epsilon x_1 + \epsilon^2 x_2$.

A. Solution at order ϵ^0

As before, our governing equation to order ϵ^0 is

$$\ddot{x}_0 + \omega^2 x_0 = 0, \tag{S46}$$

with solution

$$x_0 = \frac{1}{2} A_0 e^{i\omega t} + \text{c.c.}, \tag{S47}$$

where the complex amplitude A_0 will be determined by subsequent levels of perturbation theory.

B. Solution at order ϵ^1

Equation S45 written to order ϵ^1 is:

$$\begin{aligned} \ddot{x}_1 + \omega^2 x_1 &= -\alpha_2 x_0^2 \\ &= -\frac{\alpha_2}{4}\left[A_0^2 e^{i2\omega t} + \text{c.c.}\right] - \frac{\alpha_2 |A_0|^2}{2}, \end{aligned} \tag{S48}$$

where, again, c.c. is the conjugate of the preceding terms (in this case, c.c. = $A_0^{*2}e^{-i2\omega t}$).

The general solution of the above equation is

$$x_1 = \frac{1}{2}A_1 e^{i\omega t} + \frac{1}{2}B_1 e^{i2\omega t} + \text{c.c.} + \delta_{x1}, \tag{S49}$$

where δ_{x1} is a constant. A_1 cannot yet be determined, but the remaining terms are given by substituting into Eq. S48:

$$B_1 = \frac{\alpha_2 A_0^2}{6\omega^2} \tag{S50}$$

$$\delta_{x1} = -\frac{\alpha_2 |A_0|^2}{2\omega^2}. \tag{S51}$$

Note that unlike the case of a purely cubic nonlinearity (considered in Section S4), when a quadratic nonlinearity is introduced x undergoes a shift in equilibrium position (given by δ_{x1} above) and motion at even harmonics of the drive frequency (e.g. B_1 above) as well as odd harmonics.

C. Solution at order ϵ^2

Equation S45 written at order ϵ^2 is:

$$\ddot{x}_2 + \omega^2 x_2 = -2\alpha_2 x_0 x_1 + \left(\omega^2 - \omega_0^2\right) x_0 - \gamma \dot{x}_0 - \alpha_3 x_0^3 + \kappa \cos \omega t. \tag{S52}$$

Upon substituting our solutions for x_0 and x_1, this becomes:

$$\begin{aligned} \ddot{x}_2 + \omega^2 x_2 =& \frac{1}{2}\left\{\left[\omega^2 - \omega_0^2 - i\omega\gamma - \frac{3}{4}\alpha_3 |A_0|^2\right] A_0 - \alpha_2 \left(2A_0\delta_{x1} + A_0^* B_1\right) + \kappa\right\} e^{i\omega t} \\ & - \frac{1}{2}\alpha_2 A_0 A_1 e^{i2\omega t} - \frac{1}{2}\left[\alpha_2 A_0 B_1 + \frac{1}{4}\alpha_3 A_0^3\right] e^{i3\omega t} - \frac{1}{2}\alpha_2 A_0^* A_1 + \text{c.c.}. \end{aligned} \tag{S53}$$

Setting the secular terms (terms in curly brackets) to zero and substituting in the values of δ_{x1} and B_1 leads to

$$\left[\omega^2 - \omega_0^2 - i\omega\gamma - \frac{3}{4}\alpha_3 |A_0|^2\right] A_0 - \frac{\alpha_2^2 |A_0|^2 A_0}{\omega^2}\left(-1 + \frac{1}{6}\right) + \kappa = 0, \tag{S54}$$

or

$$\left[\omega^2 - \omega_0^2 - i\omega\gamma - \frac{3}{4}\left(\alpha_3 - \frac{10\alpha_2^2}{9\omega^2}\right)|A_0|^2\right] A_0 + \kappa = 0, \tag{S55}$$

which is identical to Equation S12 in Section S4, but with $(\alpha_3 - (10\alpha_2^2)/(9\omega^2))$ replacing α. Solving for A_0 gives

$$A_0 = \frac{-\kappa}{\omega^2 - \omega_0^2 - \frac{3}{4}\left(\alpha_3 - \frac{10\alpha_2^2}{9\omega^2}\right)|A_0|^2 - i\omega\gamma}. \tag{S56}$$

As with Eq. S14, given our initial assumption of small detuning $\sigma = (\omega - \omega_0)$, this is equivalent to

$$A_0 = \frac{-\kappa/(2\omega_0)}{\omega - \omega_{\mathrm{NL}} - i\gamma/2}, \tag{S57}$$

where

$$\omega_{\mathrm{NL}} = \omega_0 + \frac{3|A_0|^2}{8\omega_0}\left(\alpha_3 - \frac{10\alpha_2^2}{9\omega_0^2}\right) \tag{S58}$$

describes the nonlinear coupling between the resonant frequency and $|A_0|$.

The solution to Eq. S53 is

$$x_2 = \frac{1}{2}A_2 e^{i\omega t} + \frac{1}{2}B_2 e^{i2\omega t} + \frac{1}{2}C_2 e^{i3\omega t} + \text{c.c.} + \delta_{x2}, \tag{S59}$$

where

$$B_2 = \frac{\alpha_2}{3\omega^2}A_0 A_1 \tag{S60}$$

$$C_2 = \frac{1}{8\omega^2}\left[\alpha_2 A_0 B_1 + \frac{1}{4}\alpha_3 A_0^3\right] = \frac{A_0^3}{32\omega^2}\left[\frac{2\alpha_2^2}{3\omega^2} + \alpha_3\right] \tag{S61}$$

$$\delta_{x2} = -\frac{\alpha_2}{2\omega^2}\left(A_0^* A_1 + A_0 A_1^*\right), \tag{S62}$$

and A_1, A_2 are still undetermined.

D. Solution at order ϵ^3

Equation S45 written at order ϵ^3 is:

$$\ddot{x}_3 + \omega^2 x_3 = -\alpha_2(2x_0x_2 + x_1^2) + (\omega^2 - \omega_0^2)x_1 - \gamma\dot{x}_1 - 3\alpha_3 x_0^2 x_1. \tag{S63}$$

Based on our results at order ϵ and ϵ^2, We suspect that the highest frequency term of x_3 will oscillate at frequency 4ω. Therefore, we will concern ourselves primarily with evaluating x_3 at this frequency. We will not be concerned with lower frequency terms (LFT), since they will only add small corrections to the solutions we have already obtained in x_0, x_1, and x_2.

First, we will substitute Eqs. S47, S49, and S59 into the products x_0x_2, x_1^2, and $x_0^2x_1$ to give:

$$x_0x_2 = \frac{1}{4}\left(A_0C_2e^{i4\omega t} + c.c.\right) + \text{LFT} \tag{S64}$$

$$x_1^2 = \frac{1}{4}\left(B_1^2e^{i4\omega t} + c.c.\right) + \text{LFT} \tag{S65}$$

$$x_0^2x_1 = \frac{1}{8}\left(A_0^2B_1e^{i4\omega t} + c.c.\right) + \text{LFT}. \tag{S66}$$

Substituting these into Eq. S63 then results in:

$$\ddot{x}_3 + \omega^2x_3 = -\frac{1}{4}\left[\alpha_2(2A_0C_2 + B_1^2) + \alpha_3\frac{3}{2}A_0^2B_1\right]e^{i4\omega t} + c.c. + \text{LFT}. \tag{S67}$$

The general solution for x_3 will be

$$x_3 = \frac{1}{2}A_3e^{i\omega t} + \frac{1}{2}B_3e^{i2\omega t} + \frac{1}{2}C_3e^{i3\omega t} + \frac{1}{2}D_3e^{i4\omega t} + c.c. + \delta_{x3}, \tag{S68}$$

where

$$\begin{aligned} D_3 &= \frac{1}{30\omega^2}\left[\alpha_2(2A_0C_2 + B_1^2) + \alpha_3\frac{3}{2}A_0^2B_1\right] \\ &= \frac{\alpha_2A_0^4}{96\omega^4}\left[\frac{2\alpha_2^2}{9\omega^2} + \alpha_3\right], \end{aligned} \tag{S69}$$

which is found upon substituting Eq. S50 for B_1 and Eq. S61 for C_2.

E. Summary

In summary, the solution of the driven, damped oscillator with cubic and quadratic nonlinearities is

$$x = \frac{1}{2}Ae^{i\omega t} + \frac{1}{2}Be^{i2\omega t} + \frac{1}{2}Ce^{i3\omega t} + \frac{1}{2}De^{i4\omega t} + \text{c.c} + \delta_x, \tag{S70}$$

where

$$A = A_0 + A_1 + A_2 + \ldots \tag{S71}$$

$$B = B_1 + B_2 + \ldots \tag{S72}$$

$$C = C_2 + \ldots \tag{S73}$$

$$D = D_3 + \ldots \tag{S74}$$

$$\delta_x = \delta_{x1} + \delta_{x2} + \ldots \tag{S75}$$

Compared to the case of a driven oscillator with only a cubic nonlinearity (derived in Section S4), adding a quadratic nonlinearity introduces the following complications:

1. The oscillator experiences a shift δ_x to its equilibrium position.

2. The oscillator motion has frequency components at all integer harmonics of the drive frequency ω, rather than only odd integers.

3. To lowest order, the observed frequency peak is qualitatively similar, but with a "nonlinear resonant frequency" ω_{NL} given by Eq. S58. Note that α_2 is squared in this expression, meaning that no matter the sign of α_2, it will always serve to soften the nonlinear frequency peak (tilt the peak toward lower frequencies).

We infer that the solutions we have obtained for δ_{x1}, B_1, and C_2 are stable following a similar argument to that used in Sec. S4.

To lowest order, the relative magnitudes of the first and second harmonics are given by Equation S50:

$$\frac{|B_1|}{|A_0|} = \frac{|\alpha_2|\,|A_0|}{6\omega^2}. \tag{S76}$$

Similarly, the relative magnitudes of the equilibrium shift δ_x and the first harmonic are given by Equation S51:

$$\frac{|\delta_{x1}|}{|A_0|} = \frac{|\alpha_2|\,|A_0|}{2\omega^2}. \tag{S77}$$

So the relative magnitude of the second harmonic can be estimated from:

$$\frac{|B_1|}{|A_0|} = \frac{1}{3}\frac{|\delta_{x1}|}{|A_0|}. \tag{S78}$$

Therefore if δ_x and A are known, the second harmonic B can be estimated. With this in hand, we can estimate the third harmonic C using the nonlinear resonant frequency shift $\Delta\omega = \omega_{\mathrm{NL}} - \omega_0$. The normalized frequency shift is

$$\frac{\Delta\omega}{\omega_0} = \frac{3|A_0|^2}{8\omega_0^2}\left(\alpha_3 - \frac{10\alpha_2^2}{9\omega_0^2}\right). \tag{S79}$$

Meanwhile, C can be estimated using C_2:

$$\begin{aligned}\frac{|C_2|}{|A_0|} &= \frac{|A_0|^2}{32\omega^2}\left|\frac{2\alpha_2^2}{3\omega^2} + \alpha_3\right| \\ &\approx \frac{|A_0|^2}{32\omega_0^2}\left|\frac{2\alpha_2^2}{3\omega_0^2} + \alpha_3\right|,\end{aligned} \tag{S80}$$

where we have again made explicit use of the small detuning assumption. This equation can be written in terms of $\Delta\omega$ and δ_{x1} by solving Eq. S77 for α_2, solving Eq. S79 for α_3, and

substituting these into Eq. S80. The result is:

$$\frac{|C_2|}{|A_0|} \approx \left| \frac{1}{12} \frac{\Delta\omega}{\omega_0} + \frac{2}{9} \left(\frac{\delta_{x1}}{|A_0|} \right)^2 \right|. \tag{S81}$$

When $\alpha_2 = 0$, we have $\delta_{x1} = 0$ and the above result reproduces Eq. S42. By repeating this process with Eq. S69, one can show that the leading term at frequency 4ω has a relative amplitude of:

$$\frac{|D_3|}{|A_0|} \approx \frac{1}{18} \frac{|\delta_{x1}|}{|A_0|} \left| \frac{\Delta\omega}{\omega_0} + 2 \left(\frac{\delta_{x1}}{|A_0|} \right)^2 \right|, \tag{S82}$$

which equals zero when $\alpha_2 = 0$.

As a final note, we'll comment on the phases of the harmonics B, C, and D relative to the fundamental tone A. The lowest-order solutions for each of these harmonics gives

$$x = \frac{1}{2} A_0 e^{i\omega t} + \frac{1}{2} B_1 e^{i2\omega t} + \frac{1}{2} C_2 e^{i3\omega t} + \frac{1}{2} D_3 e^{i4\omega t} + \text{c.c.} + \delta_{x1}, \tag{S83}$$

where δ_{x1} is real and A_0, B_1, C_2, D_3 are complex. According to Eqs. S50, S61, and S69, we have $B_1 \propto A_0^2$, $C_2 \propto A_0^3$, and $D_3 \propto A_0^4$, where the proportionality constants are always real. Thus if we express the fundamental as $A_0 = |A_0| e^{i\theta}$, the arguments of B_1, C_2, and D_3 will always be $2\theta, 3\theta$, and 4θ, respectively. Therefore we can rewrite the above equation as:

$$x = \frac{1}{2} |A_0| e^{i(\omega t + \theta)} + \frac{1}{2} |B_1| e^{i2(\omega t + \theta)} + \frac{1}{2} |C_2| e^{i3(\omega t + \theta)} + \frac{1}{2} |D_3| e^{i4(\omega t + \theta)} + \text{c.c.} + \delta_{x1}. \tag{S84}$$

This shows the inherent relation between the phases of the harmonics of motion. If $t = 0$ is redefined so that the fundamental harmonic is a pure cosine, the higher harmonics will also be pure cosines. This assertion is valid to lowest order in B, C, and D.

* robert.ilic@nist.gov

[1] H. R. Philipp, Journal of The Electrochemical Society **120**, 295 (1973).

[2] D. E. Aspnes and A. A. Studna, Physical Review B **27**, 985 (1983).

[3] C. H. Metzger and K. Karrai, Nature **432**, 1002 (2004).

[4] R. A. Barton, I. R. Storch, V. P. Adiga, R. Sakakibara, B. R. Cipriany, B. Ilic, S. P. Wang, P. Ong, P. L. McEuen, J. M. Parpia, and H. G. Craighead, Nano Letters **12**, 4681 (2012).

[5] R. De Alba, T. S. Abhilash, R. H. Rand, H. G. Craighead, and J. M. Parpia, Nano Letters **17**, 3995 (2017).

[6] M. Zalalutdinov, K. L. Aubin, M. Pandey, A. T. Zehnder, R. H. Rand, H. G. Craighead, J. M. Parpia, and B. H. Houston, Applied Physics Letters **83**, 3281 (2003).

[7] K. Aubin, M. Zalalutdinov, T. Alan, R. B. Reichenbach, R. Rand, A. Zehnder, J. Parpia, and H. Craighead, Journal of Microelectromechanical Systems **13**, 1018 (2004).

[8] M. Pandey, K. Aubin, M. Zalalutdinov, R. B. Reichenbach, A. T. Zehnder, R. H. Rand, and H. G. Craighead, Journal of Microelectromechanical Systems **15**, 1546 (2006).

[9] D. B. Blocher, A. T. Zehnder, and R. H. Rand, Journal of Microelectromechanical Systems **22**, 835 (2013).

[10] V. N. Mahajan, Journal of the Optical Society of America **73**, 860 (1983).

[11] A. H. Nayfeh and D. T. Mook, *Nonlinear Oscillations* (Wiley-VCH, 1995).

[12] R. H. Rand, "Lecture notes on nonlinear vibrations," (2012), PDF document retrieved from Cornell eCommons website: https://hdl.handle.net/1813/28989.